

# A hadronic origin for ultra-high-frequency-peaked BL Lac objects

M. Cerruti,<sup>1</sup> A. Zech,<sup>2</sup> C. Boisson,<sup>2</sup> S. Inoue<sup>3,4</sup>

<sup>1</sup> *Harvard-Smithsonian Center for Astrophysics, 60 Garden Street, Cambridge MA, 02138, USA*  
*matteo.cerruti@cfa.harvard.edu*

<sup>2</sup> *LUTH, Observatoire de Paris, CNRS, Université Paris Diderot, PSL Research University; 5 Place Jules Janssen, 92190 Meudon, France*  
*andreas.zech@obspm.fr*

<sup>3</sup> *Institute for Cosmic Ray Research, 5-1-5 Kashiwanoha, Kashiwa, Chiba 277-8582, Japan*

<sup>4</sup> *Max-Planck-Institut für Physik, Föhringer Ring 6, 80805 München, Germany*

February 13, 2015

## ABSTRACT

Current Cherenkov telescopes have identified a population of ultra-high-frequency peaked BL Lac objects (UHBLs), also known as extreme blazars, that exhibit exceptionally hard TeV spectra, including 1ES 0229+200, 1ES 0347-121, RGB J0710+591, 1ES 1101-232, and 1ES 1218+304. Although one-zone synchrotron-self-Compton (SSC) models have been generally successful in interpreting the high-energy emission observed in other BL Lac objects, they are problematic for UHBLs, necessitating very large Doppler factors and/or extremely high minimum Lorentz factors of the emitting leptonic population. In this context, we have investigated alternative scenarios where hadronic emission processes are important, using a newly developed (lepto-)hadronic numerical code to systematically explore the physical parameters of the emission region that reproduces the observed spectra while avoiding the extreme values encountered in pure SSC models. Assuming a fixed Doppler factor  $\delta = 30$ , two principal parameter regimes are identified, where the high-energy emission is due to: 1) proton-synchrotron radiation, with magnetic fields  $B \sim 1 - 100$  G and maximum proton energies  $E_{p,max} \lesssim 10^{19}$  eV; and 2) synchrotron emission from p- $\gamma$ -induced cascades as well as SSC emission from primary leptons, with  $B \sim 0.1 - 1$  G and  $E_{p,max} \lesssim 10^{17}$  eV. This can be realized with plausible, sub-Eddington values for the total (kinetic plus magnetic) power of the emitting plasma, in contrast to hadronic interpretations for other blazar classes that often warrant highly super-Eddington values.

**Key words:** Astroparticle Physics; Relativistic Processes; Galaxies : blazars; Galaxies : individual : 1ES 0229+200, 1ES 0347-121, RGB J0710+591, 1ES 1101-232, 1ES 1218+304

## 1 INTRODUCTION

Blazars are a class of active galactic nuclei (AGN) characterized by predominantly non-thermal spectra at all wavelengths, from radio to  $\gamma$ -rays, relatively weak (or absent) optical/UV emission lines, rapid variability and a high degree of polarization (Stein et al. 1976; Moore & Stockman 1981). These observational properties can be consistently interpreted in the context of the unified AGN model (Urry & Padovani 1995), assuming that blazars are radio-loud AGN, with relativistic jets pointed nearly towards the observer. Their spectral energy distribution (SED) is thus dominated by the Doppler-boosted non-thermal emission from the jet. Multi-wavelength observations have shown that blazar SEDs generally exhibit two bumps, one peaking at low energies (infrared to X-rays), and one peaking in  $\gamma$ -rays (see e.g. Abdo et al. 2010).

The origin of the low-energy bump is commonly ascribed to synchrotron emission from relativistic electrons in an emitting re-

gion located inside the jet, approaching relativistically towards the observer.

The origin of the high-energy bump is still under debate. In leptonic models, the high-energy emission is supposed to be inverse Compton emission from relativistic electrons that up-scatter either low-energy synchrotron photons emitted by the same population of electrons (synchrotron-self-Compton model, SSC, e.g. Konigl 1981), or photons originating from outside the jet (external-inverse-Compton, EIC, e.g. Sikora et al. 1994) such as the thermal emission from the accretion disk, the dusty torus, the broad-line region (BLR), or from stellar clusters located near the blazar emitting region. In hadronic models the high energy bump is instead assumed to originate from protons accelerated to ultra-high energies in the jet, via either the synchrotron photons radiated by the protons, or emission from secondary particles such as electron-positron pairs or muons generated in p- $\gamma$  interactions of the protons with low-energy internal and/or external photon fields (e.g. Mannheim 1993;

Dermer & Atoyan 2001; Mücke & Protheroe 2001, hereafter M01). For a recent modeling attempt of *Fermi*-LAT blazars in both leptonic and hadronic scenarios, see Böttcher et al. (2013).

In an alternative scenario, protons or neutrons escaping from the emitting region trigger intergalactic cascades with the extragalactic background light (EBL) or cosmic microwave background (CMB) (e.g. Essey & Kusenko 2010; Dermer et al. 2012; Murase et al. 2012).

Proton-proton interactions (important in denser environments, such as supernovae remnants or micro-quasars, see e.g. Ackermann et al. 2013b; Romero et al. 2003, respectively) are commonly neglected in blazar hadronic models, because the particle density in the emitting region is considered too low for them to be important (see however Reynoso et al. 2011). An exception to this are models based on the interaction of relativistic protons inside the jet with stellar envelopes or gas clouds (e.g. Barkov et al. 2010).

Ninety percent of the AGN detected so far with ground-based Cherenkov telescope arrays, i.e. at very high energies (VHE) above  $\sim 100$  GeV, are blazars of the BL Lac type<sup>1</sup>. They can be further classified according to the frequency of the first SED peak (Padovani & Giommi 1995) into high-frequency-peaked BL Lac objects (HBLs, peaking in X-rays), or intermediate and low-frequency-peaked BL Lac objects (IBLs and LBLs, peaking in optical-infrared). Due to their hard spectra, HBLs currently account for the largest fraction of “TeV-loud” AGN (75%). Out of the 44 HBLs detected so far in the TeV range, five sources — IES 0229+200, IES 0347-121, RGB J0710+591, IES 1101-232 and IES 1218+304 — are characterized by particularly hard spectra with the high-energy peak above  $\sim 1$  TeV, which is consistent with their very hard and weak signal in the *Fermi*-LAT band. Another common characteristic is the lack of observable variability on short time-scales of the very-high-energy flux (with the exception of IES 1218+304, which showed VHE flaring activity on the scale of days, Acciari et al. 2010a). Although the BL Lac object H 1426+428 belongs to this sub-class as well, since it was detected at VHE only during flaring activity without extensive multi-wavelength coverage (Aharonian et al. 2002; Djannati-Ataï et al. 2002; Horan et al. 2002; Petry et al. 2002; Leonardo et al. 2009; Benbow 2011) we decided to exclude it from our sample.

The modelling of these ultra-high-frequency peaked BL Lacs (UHBLs, also known as extreme BL Lacs, EHBLs, see e.g. Costamante et al. 2001; Şentürk et al. 2013, for a more recent review) with one-zone SSC scenarios, which usually yield good results for HBLs, is proving difficult in most cases, as can be seen from Table 1, where some recent attempts at SSC modeling of the sources are summarized. A good representation of the complete SEDs requires either extremely high values of the minimum Lorentz factor of the electron distribution (IES 1101-232, IES 0347-121), or an elevated Doppler factor (IES 1218+304), or both (IES 0229+200, RGB J0710+591). Very large Doppler factors imply either a very fast movement of the plasma blob and/or a very small viewing angle with respect to the jet axis and could thus be difficult to reconcile with radio observations of the movement of knots inside jets (see e.g. Lister et al. 2013) or with the statistics of observed blazars and radio-galaxies (Henri & Saugé 2006).

A very high value of  $\gamma_{min}$ , and thus a very narrow stationary electron energy distribution, requires specific and finely-tuned conditions to occur. It might arise if electrons can somehow be injected into the emission region with a narrow energy distribution,

and their subsequent cooling is inefficient, or if the cooling of particles accelerated at a shock is compensated by stochastic turbulent re-acceleration (Katarzyński et al. 2006; Lefa et al. 2011; Asano et al. 2014).

Another possibility to achieve very hard VHE spectra with high minimum electron energies is given by models including external Compton upscattering of ambient photon fields (Lefa et al. 2011), which are however generally thought to dominate in powerful flat-spectrum-radio-quasars (FSRQs) and LBLs (see e.g. Meyer et al. 2012b), but not in HBLs, in view of the absence of a detectable emission from the accretion disk or the BLR in these sources. The above mentioned intergalactic cascades may also provide a hard spectral component at the highest energies to fit the spectra of UHBLs, as was shown for example for IES 0229+200 by Murase et al. (2012).

A hadronic origin of the TeV spectrum of IES 1101-232 has recently been proposed by Cao & Wang (2014). They ascribe the spectrum measured with the H.E.S.S. Cherenkov telescopes from this source to secondary  $\gamma$ -ray emission from neutral pion decay following interactions of sub-PeV protons with synchrotron radiation inside the source. This interpretation, however, requires an extremely large power in protons of a few  $10^{53}$  erg s<sup>-1</sup>, around six orders of magnitudes higher than the Eddington luminosity of the super-massive black hole (SMBH) powering the AGN.

In this paper, we systematically investigate a global interpretation of the SEDs of the five UHBLs within a (lepto-)hadronic framework. By ascribing the low-energy and high-energy bumps in the SEDs to different particle populations, sharing however a common acceleration and emission region, extreme values for the Doppler factor and the minimum electron Lorentz factor can be avoided. We show that two distinct sets of solutions with acceptable power requirements can be found in this way. In general, hadronic scenarios have the added benefit of providing a potential link to the outstanding question of the sources of ultra-high energy cosmic rays (UHECRs, see Kotera & Olinto 2011, for a recent review), as well as possibly the sources of PeV neutrinos recently discovered (IceCube Collaboration 2013).

In Sec. 2 we present a new stationary code, which computes both the leptonic and hadronic components and permits the study of a much wider parameter space than the standard SSC or hadronic codes. In particular, leptonic or hadronic scenarios can be evaluated in a consistent framework, by simply varying the physical parameters of the emitting region (i.e. its particle content and its magnetic energy density). Interesting mixed — “lepto-hadronic” — scenarios, in which the high energy bump has comparable contributions from both SSC and proton-induced cascade emission, naturally arise in this framework. In its current form, the code is focused on the interpretation of emission from (U)HBLs: in particular, we do not consider external photon fields which are thought to be important in flat-spectrum radio quasars (FSRQs) and probably in LBLs.

In Sec. 3 we present, as an example, a first application of our code to the well-studied HBL Mrk 421 and compare our results to those of a previously published, independent hadronic code.

In Sec. 4 we focus on the systematic application of our code to the five UHBLs. By scanning the parameter space of all acceptable values of the strength of the magnetic field and the size of the emission region for a given Doppler factor, we arrive at two separate regions of solutions with distinct ranges for these parameters. The first set of solutions is dominated by proton-synchrotron emission, while the other is dominated by synchrotron emission from pair cascades triggered by hadronic interactions plus SSC emission from the pri-

<sup>1</sup> <http://tevcat.uchicago.edu>

object	z	SSC parameters	VHE variability	Log( $M_{\bullet}/M_{\odot}$ )
1ES 0229+200	0.140	$\delta=50$ , $B=0.4$ G, $R=54 \times 10^{15}$ cm, $\gamma_{min}=5 \times 10^5$ (Tavecchio et al. 2009); $\delta=40$ , $B=0.032$ G, $R=10^{18}$ cm, $\gamma_{min}=4 \times 10^5$ (Kaufmann et al. 2011); $\delta > 53$ , $B=0.8-3.3$ mG, $R=(5-30) \times 10^{15}$ cm, $\gamma_{min}=(2.5-4.5) \times 10^4$ (Aliu et al. 2014);	indication for variability on time scales of years (Aliu et al. 2014)	$9.16 \pm 0.11$
1ES 0347-121	0.188	$\delta=25$ , $B=0.035$ G, $R=3.2 \times 10^{16}$ cm, $\gamma_{min}=10^3$ (Aharonian et al. 2007b) $\delta=61$ , $B=1.3$ mG, $R=1.6 \times 10^{17}$ cm, $\gamma_{min}=2 \times 10^4$ (Tanaka et al. 2014);	no known variability	$8.02 \pm 0.11$
RGB J0710+591	0.125	$\Gamma=30$ , $B=0.036$ G, $R=2 \times 10^{16}$ cm, $\gamma_{min}=6 \times 10^4$ (Acciari et al. 2010b);	no known variability	$8.25 \pm 0.22$
1ES 1101-232	0.186	$\delta=25$ , $B=0.1$ G, $R \approx 10^{16}$ cm, $\gamma_{min}=10^3$ (Aharonian et al. 2007a);	no known variability	9
1ES 1218+304	0.184	$\delta=80$ , $B=0.04$ G, $R=3 \times 10^{15}$ cm (Rüger et al. 2010); $\delta=44$ , $B=0.12$ G, $R=3 \times 10^{15}$ cm (Weidinger & Spanier 2010);	variability on the scale of days (Acciari et al. 2010a)	$8.04 \pm 0.24$

**Table 1.** Characterization of the five UHBLs with one-zone SSC models. The model parameters are: the Doppler factor ( $\delta$ ) or bulk Lorentz factor ( $\Gamma$ ); the magnetic field  $B$ ; the size of the emission region  $R$ ; the minimum Lorentz factor  $\gamma_{min}$  of the primary electron distribution. The references for the redshift measurements are Woo et al. (2005) for both 1ES 0229+200 and 1ES 0347-121, Falomo et al. (2003) for RGB J0710+591, Remillard et al. (1989) for 1ES 1101-232, and Ahn et al. (2012) for 1ES 1218+304. The masses of the super-massive black-holes are taken from Aharonian et al. (2007b) (for 1ES 0347-121) and Meyer et al. (2012a) (for the remaining objects). For 1ES 1101-232, in absence of a reliable mass estimation, we considered a standard average value of  $10^9 M_{\odot}$ .

mary leptons.

The implication on the source physics of the solutions found with this parameter scan are discussed in Sec. 5. We focus specifically on the viability of the solutions with respect to the required jet power. We also study the constraints our solutions pose on the acceleration processes, the expected flux variability and a potential connection with UHECRs.

## 2 DESCRIPTION OF THE CODE

### 2.1 Leptonic processes

The leptonic part of the code we present here is a direct evolution of the SSC code developed by Katarzyński et al. (2001) (hereafter K01): a spherical emitting region of radius  $R$ , moving with Doppler factor  $\delta$  in a relativistic jet with angle  $\theta$  to the line of sight, is filled with a tangled, homogeneous magnetic field with amplitude  $B$  and a stationary population of primary electrons described by  $N_e(\gamma_e)$ .<sup>2</sup> Here  $\gamma_e = E_e/mc^2$  is the Lorentz factor of the electrons,  $N_e(\gamma_e) d\gamma_e$  representing the number of electrons per unit volume with a Lorentz factor between  $\gamma_e$  and  $\gamma_e + d\gamma_e$ . A break in the stationary electron distribution is expected as a consequence of the cooling of the particles via synchrotron emission and inverse Compton scattering, see e.g. Inoue & Takahara (1996). The electron energy distribution is thus described by a broken power-law function, defined by the two slopes  $\alpha_{e,1}$  and  $\alpha_{e,2}$ , the Lorentz factors  $\gamma_{e,min}$ ,  $\gamma_{e,break}$  and  $\gamma_{e,max}$ , and a normalization factor  $K_e$ .

The synchrotron emission is evaluated using the standard relativistic formulae for the emissivity and self-absorption (see

for example Rybicki & Lightman 1979); the inverse Compton emission is evaluated using the Compton kernel given by Jones (1968), which correctly describes the Comptonized spectrum in both the Thomson and the Klein-Nishina regimes.

High-energy photons are absorbed by the pair-production process ( $\gamma + \gamma' \rightarrow e^+ + e^-$ ) after interaction with the low-energy synchrotron photons inside the emitting region, which can modify the observed  $\gamma$ -ray spectrum (see e.g. Aharonian et al. 2008). In general, a more significant effect is  $\gamma$ - $\gamma$  pair production with the infrared photons of the extragalactic background light (EBL) experienced by the high-energy photons traveling from the source towards the Earth (Salamon & Stecker 1998). Both effects are included in the code described by K01.

Several modifications and improvements have been applied to the original leptonic code:

- The stationary distribution of primary electrons has been modified, replacing the sharp cut-off at the maximum energy ( $N_e(\gamma_e) = 0$  if  $\gamma_e > \gamma_{e,max}$ ) with a more natural exponential cut-off:

$$N_e(\gamma_e) = \begin{cases} K_e \gamma_e^{-\alpha_{e,1}} e^{-\gamma_e/\gamma_{e,max}} & \text{if } \gamma_{e,min} \leq \gamma_e < \gamma_{e,break} \\ \gamma_{e,break}^{\alpha_{e,2}-\alpha_{e,1}} K_e \gamma_e^{-\alpha_{e,2}} e^{-\gamma_e/\gamma_{e,max}} & \text{if } \gamma_{e,break} \leq \gamma_e \end{cases} \quad (1)$$

where  $K_e$  is the normalization factor of the electron distribution, in  $\text{cm}^{-3}$ .

- The computation of the synchrotron emission has been improved in precision by performing the complete integration over the pitch angle between the charged particle and the magnetic field, while in the original code this integral was approximated by a simple analytical function (see K01, appendix A), evaluated in a well defined energy range. This modification is unavoidable for a hadronic extension of the code that includes proton synchrotron

<sup>2</sup> This population can be interpreted as consisting of electrons and positrons, but we will refer to it simply as "electrons" in the following.

emission, as will be discussed below. The synchrotron emissivity  $j(\nu)$  (in  $\text{erg s}^{-1} \text{cm}^{-3} \text{Hz}^{-1} \text{sterad}^{-1}$ ) is now evaluated as:

$$j(\nu) = \frac{1}{8\pi} \int_0^\pi d\vartheta \sin \vartheta \int_{\gamma_{e,\min}}^\infty d\gamma_e N_e(\gamma_e) P(\nu, \gamma_e, \vartheta) \quad (2)$$

where  $P(\nu, \gamma_e, \vartheta)$  is the power emitted by each electron (in  $\text{erg s}^{-1} \text{Hz}^{-1} \text{sterad}^{-1}$ ), equal to:

$$P(\nu, \gamma_e, \vartheta) = \frac{\sqrt{3}e^3 B \sin \vartheta}{m_e c^2} \frac{\nu}{\nu_c} \int_{\frac{\nu}{\nu_c}}^\infty dx K_{5/3}(x) \quad (3)$$

where  $\nu_c = (3eB/(4\pi m_e c)) \gamma_e^2 \sin \vartheta$  and  $K_j(x)$  is the modified Bessel function of the second kind of order  $j$ . To reduce the computing time of the code, the integral  $I(a) = \int_a^\infty dx K_{5/3}(x)$  has been tabulated, and then a linear interpolation as a function of  $a$  is performed.

- The evaluation of the absorption due to internal  $\gamma - \gamma$  pair production has been modified, replacing the simple cross-section  $\delta$ -function approximation with the formula given by Aharonian et al. (2008), yielding a better accuracy:

$$\sigma_{\gamma\gamma} = \frac{3}{2} \frac{\sigma_T}{s^2} \left[ \left( s + \frac{1}{2} \ln s - \frac{1}{6} + \frac{1}{2s} \right) \ln(\sqrt{s} + \sqrt{s-1}) + \right. \\ \left. - \left( s + \frac{4}{9} - \frac{1}{9s} \right) \sqrt{1 - \frac{1}{s}} \right] \quad (4)$$

where  $s$  represents the normalized, non-dimensional product of the energies of the primary and target photons ( $E$  and  $E'$ ):  $s = EE'/(m_e^2 c^4)$ .

- The secondary population of leptons coming from  $\gamma - \gamma$  pair production is computed using the injection function  $Q_e(\gamma_e) d\gamma_e$  (defined as the number of injected pairs per unit volume and time, with a Lorentz factor between  $\gamma_e$  and  $\gamma_e + d\gamma_e$ ) given by Aharonian et al. (1983):

$$Q_e(\gamma_e) = \frac{3\sigma_{TC}}{32} \int_{\gamma_e}^\infty d\varepsilon \frac{n_e(\varepsilon)}{\varepsilon^3} \int_{\frac{\varepsilon}{4\gamma_e(\varepsilon-\gamma_e)}}^\infty d\varepsilon' \frac{n_{e'}(\varepsilon')}{\varepsilon'^2} \cdot \\ \cdot \left[ \frac{4\varepsilon^2}{\gamma_e(\varepsilon-\gamma_e)} \ln \left( \frac{4\gamma_e \varepsilon' (\varepsilon - \gamma_e)}{\varepsilon} \right) - 8\varepsilon \varepsilon' + \right. \\ \left. + \frac{2\varepsilon^2(\varepsilon \varepsilon' - 1)}{\gamma_e(\varepsilon - \gamma_e)} - \left( 1 - \frac{1}{\varepsilon \varepsilon'} \right) \left( \frac{\varepsilon^2}{\gamma_e(\varepsilon - \gamma_e)} \right)^2 \right] \quad (5)$$

where  $\varepsilon = E/(m_e c^2)$  and  $\varepsilon' = E'/(m_e c^2)$  are the normalized, non-dimensional energies of the two photons (with  $\varepsilon \gg \varepsilon'$ ), and  $n_{e,\varepsilon'}(\varepsilon, \varepsilon')$  is the number density of photons of high ( $\varepsilon$ ) and low ( $\varepsilon'$ ) energy.

The injection function  $Q_e(\gamma_e)$  has been used as a source term in the continuity equation in order to determine the stationary state of the population of produced pairs  $N'_e(\gamma_e)$ :

$$\frac{\partial}{\partial t} N'_e(\gamma_e) = \frac{\partial}{\partial \gamma_e} \left[ \gamma_e \frac{N'_e(\gamma_e)}{\tau_c(\gamma_e)} \right] + Q_e(\gamma_e) - \frac{N'_e(\gamma_e)}{\tau_{ad}} \quad (6)$$

where we chose  $\tau_{ad} = 2R/c$  as the adiabatic time scale (the factor 0.5c is typical for this type of objects, see M01) and

$$\tau_c(\gamma_e) = \frac{3m_e c}{4(u_B + u_{soft})\sigma_T \gamma_e} \quad (7)$$

is the radiative cooling time, including both synchrotron losses ( $u_B$  being the magnetic energy density) and inverse-Compton losses (in the Thomson regime;  $u_{soft}$  being the synchrotron photon energy

density). The stationary state has been computed using the integral expression given by Inoue & Takahara (1996):

$$N'_e(\gamma_e) = e^{-\gamma_e^*/\gamma_e} \frac{\gamma_e^* \tau_{ad}}{\gamma_e^2} \int_{\gamma_e}^\infty d\zeta Q_e(\zeta) e^{+\gamma_e^*/\zeta} \quad (8)$$

with

$$\gamma_e^* = \frac{3m_e c^2}{8(u_B + u_{soft})\sigma_T R} \quad (9)$$

representing the Lorentz factor at which  $\tau_c(\gamma_e) = \tau_{ad}$ . The associated stationary synchrotron emission is then being computed.

- The absorption by the EBL is computed using the model by Franceschini et al. (2008), which agrees well with the latest constraints obtained by very-high-energy (VHE;  $E > 100$  GeV) observations (Aharonian et al. 2006; H.E.S.S. Collaboration et al. 2013).

## 2.2 Hadronic processes

The emitting region is assumed to be filled with a stationary population of relativistic protons, in addition to the electrons. In analogy with the electron population, the proton distribution  $N_p(\gamma_p = E_p/m_p c^2)$  is described by a broken power law function:

$$N_p(\gamma_p) = \begin{cases} K_p \gamma_p^{-\alpha_{p,1}} e^{-\gamma_p/\gamma_{p,max}} & \text{if } \gamma_{p,min} \leq \gamma_p < \gamma_{p,break} \\ \gamma_{p,break}^{\alpha_{p,2}-\alpha_{p,1}} K_p \gamma_p^{-\alpha_{p,2}} e^{-\gamma_p/\gamma_{p,max}} & \text{if } \gamma_{p,break} \leq \gamma_p \end{cases} \quad (10)$$

The normalization of the proton spectrum is  $K_p = \eta K_e$ , with the  $\eta$  factor representing the ratio between the number density of protons and electrons at  $\gamma_p = \gamma_e = 1$ .

The proton synchrotron emission is evaluated in the same way as for the electrons (cf. Equations 2 and 3), by replacing the electron mass with the proton mass. When proton synchrotron photons are assumed to be responsible for the high energy bump, they suffer  $\gamma - \gamma$  absorption from both internal photons and the EBL. The  $\gamma - \gamma$  absorption and the emission from the population of secondary pairs is evaluated in analogy with what is done for the inverse Compton emission for the leptonic part of the code.

The proton population in the emitting region interacts with the low energy photons through photo-meson processes

$$p + \gamma \rightarrow p' + n^0 \pi^0 + n^+ \pi^+ + n^- \pi^- + \dots \\ \text{or} \\ p + \gamma \rightarrow n + n^0 \pi^0 + n^+ \pi^+ + n^- \pi^- + \dots \quad (11)$$

and through electron-positron pair production (Bethe-Heitler process)

$$p + \gamma \rightarrow p' + e^+ + e^- \quad (12)$$

Photo-meson production has been evaluated using the publicly available Monte-Carlo code *SOPHIA* (Mücke et al. 2000) which computes  $N_{i,er}$  interactions of a proton of energy  $E_p$  with a given low-energy photon field, and provides as output the distributions (expressed as  $E \frac{dN}{dE} = \gamma \frac{dN}{d\gamma}$ ) of the stable and long-lived particles ( $e^\pm$ ,  $\gamma$ ,  $p$ ,  $n$ ,  $\nu_{e,\mu}$  and  $\bar{\nu}_{e,\mu}$ <sup>3</sup>).

The only photon target field we consider is given by the synchrotron emission from the primary electron population in the jet,

<sup>3</sup> As the study of the neutrino emission from blazars is beyond the purposes of this paper, they will not be discussed in detail here.

which represents by far the dominant component at low energies in (U)HBLs. We slightly modified the *SOPHIA* code so that it can accept as input photon-field any numerical function (and not only a power-law or a black-body function as in the original version of the code). We call *SOPHIA* for 50 different proton energies, spaced by  $\Delta \log(\gamma_p) = 0.1$ , using for each call  $N_{iter} = 10^4$ . For the  $i$ -th call, the proton Lorentz factor is thus:

$$\log(\gamma_{p,i}) = \log(\gamma_{p,max}) - i \cdot 0.1 \quad (13)$$

The *SOPHIA* code cannot properly evaluate the energy distributions of charged secondary particles in a magnetized environment, where they can be modified by synchrotron cooling. Following M01, we thus modify the energy of the proton before interaction to account for the synchrotron losses that can occur before the proton-photon collision:

$$E'_p \simeq \frac{E_p}{1 + \frac{r_{p,syn}(E_p)}{r_\pi(E_p)}} \quad (14)$$

where  $r_{p,syn}$  represents the inverse of the proton synchrotron loss time, given by:

$$r_{p,syn}(E_p) = \frac{1}{\tau_{p,syn}(E_p)} = \frac{4}{3} \left( \frac{m_e}{m_p} \right)^2 \frac{\sigma_T u_B c}{(m_p c^2)^2} E_p \quad (15)$$

and  $r_\pi$  represents the mean pion-production interaction rate, which is evaluated using a routine integrated in *SOPHIA* (following again M01).

The *SOPHIA* output spectra are expressed as  $\gamma \frac{dN}{d\gamma}$  for each type of particle. To use them, we need to convert these spectra into injection functions, which will be then used to obtain stationary distributions. We first divide these spectra by  $\gamma$  and multiply them by  $\int_{\gamma'_{pi}}^{\gamma'_{pi+1}} d\gamma_p N'_p(\gamma_p)/\tau_{ad}$ , i.e. the rate of *injected* proton density in the emitting region with energies between  $\gamma'_{pi}$  and  $\gamma'_{pi+1}$ . Here  $N'_p(\gamma'_p)$  represents the proton distribution without spectral break and  $\gamma'_p = E'_p/m_p c^2$  is defined according to equation 14. Finally, the particle spectra are multiplied by  $r_\pi/r_{tot}$ , the ratio of the pion-production interaction rate over the total interaction rate, given by  $r_\pi + r_{BH} + 1/\tau_{ad}$ , where  $r_{BH}$  represents the Bethe-Heitler interaction rate (see equation 2.2 in Chodorowski et al. 1992). In this stationary framework, the protons are assumed to be confined in the emitting region, and multiple  $p$ - $\gamma$  interactions may occur, which are evaluated as suggested in M01. The stationary distributions of electrons and positrons are then computed following Equation 8, while the stationary distribution of photons is obtained simply by multiplying their injection rate by  $\tau_{ad}$ .

Photons from the  $\pi^0$  decay and the synchrotron emission from  $e^\pm$  coming from the  $\pi^\pm$  channel can reach energies up to  $m_p c^2 \gamma_{p,max}$ . Interacting with the low-energy photon field, they trigger electro-magnetic cascades, mediated by synchrotron emission and  $e^\pm$  pair production. The stationary state of the cascade emission is evaluated as follows: the first generation of pairs injected into the emitting region is treated in the same way as in the leptonic part of the code, by computing the injection rate, the stationary state of pair distribution and the associated synchrotron emission. In this case however, the synchrotron photons from pairs are still energetic enough to produce a second generation of pairs, which in their turn can produce a third generation, and so on. We iterate the process until the  $i$ -th generation of pairs gives a negligible contribution to the sum of the previous generations. As a general rule, for the physical parameters used in the following applications, the spectrum computed including five generations of

pairs already provides a good description of the cascade. During the computation of the cascade spectrum, the low energy photon field is considered as being represented only by the synchrotron emission of primary electrons, neglecting the emission from the cascade itself (i.e. we make the assumption that the cascade is not self-sustained, and we verify *a posteriori* that this condition is respected).

The *SOPHIA* code considers as output only stable or long-lived particles. However, in highly magnetized environments, the synchrotron emission from kaons, pions and muons before decay can be non-negligible and radiative losses can also affect the resulting spectra of electrons and positrons. Following M01, we modified the spectra of kaons, pions and muons before decay, taking into account their synchrotron losses.

Synchrotron emission from muons can significantly contribute to the overall SED for magnetic fields of the order of tens of Gauss (see e.g. Rachen 2000). We extract the muon ( $\mu^\pm$ ) spectra from *SOPHIA* before their decay into electrons and positrons, and we treat them in the same way as all the other *SOPHIA* outputs. The only difference occurs in the evaluation of the steady state distribution: for non-stable particles such as muons, we need to add the decay term (equal to  $-N(\gamma)/\gamma\tau_{dec}$ ) in Equation 6. The integral solution (equation 8) is then modified as follows:

$$N_\mu(\gamma_\mu) = \exp \left[ -\frac{\gamma_\mu^*}{\gamma_\mu} - \gamma_\mu^* \frac{\tau_{ad}}{2\gamma_\mu^2 \tau_{dec}} \right] \frac{\gamma_\mu^* \tau_{ad}}{\gamma_\mu^2} \cdot \int_{\gamma_\mu}^{\infty} d\zeta Q_\mu(\zeta) \exp \left[ +\frac{\gamma_\mu^*}{\zeta} + \gamma_\mu^* \frac{\tau_{ad}}{2\zeta^2 \tau_{dec}} \right] \quad (16)$$

where  $Q_\mu(\gamma_\mu)$  is represented by the *SOPHIA* output, and  $\gamma_\mu^*$  is the Lorentz factor at which  $\tau_c(\gamma_\mu) = \tau_{ad}$  (as in equation 9).

It should be noted that a fast alternative to the direct use of the *SOPHIA* Monte Carlo code is the approach by Kelner & Aharonian (2008), in which an analytical parametrization of the secondary particle distributions produced in the  $p$ - $\gamma$  interactions is given. However, an analytical expression for the contribution from muons does not yet exist, and in highly magnetized environments, synchrotron losses can significantly affect the distribution of secondary electrons and positrons.

A process that competes with the photo-meson channel, but is dominant at lower energies, is Bethe-Heitler pair production (which is not included in the *SOPHIA* package). The pairs injected into the emitting region through this process have been computed using the analytical formulae by Kelner & Aharonian (2008) (in which the Bethe-Heitler cross-section is expressed following the work by Blumenthal 1970). The pairs injected into the emitting region are energetic enough to trigger an electro-magnetic cascade, which is computed in the same way as for the photo-meson induced cascades.

It should be noted that our approach is different from the one used by M01, who simulated the Bethe-Heitler pair production via the Monte-Carlo code described in Protheroe & Johnson (1996).

To summarize, the hadronic component is given by seven different contributions: the synchrotron emission from protons and muons and their associated synchrotron emission from  $\gamma$ - $\gamma$  secondary pairs constitute four distinct contributions; the three remaining ones are given by the synchrotron emission from the cascades

triggered by photons produced via the  $\pi^0$  decay, by  $e^\pm$  produced via the  $\pi^\pm$  decay and by  $e^\pm$  produced via the Bethe-Heitler process.

### 2.3 Physical constraints and systematic parameter scan

In hadronic scenarios, the fact of considering an additional proton population in the emitting region leads to six more free parameters with respect to the simple SSC scenario: the three Lorentz factors  $\gamma_{p,min}$ ,  $\gamma_{p,break}$ , and  $\gamma_{p,max}$ , the indices of the proton power-law distribution  $\alpha_{p,1,2}$ , and the normalization factor  $\eta$ .

The value of  $\alpha_{p,1}$  can be constrained assuming that electrons and protons share the same acceleration mechanism in magnetic fields whose spectrum of turbulence is characterized by a single power-law at all scales, and thus have injection functions with the same index. It is fixed to  $\alpha_{e,1}$ , the index of the electron distribution before the break. This assumes that the break in the electron distribution is induced by radiative cooling and that the distribution before the break is representative of the injection spectrum. In the following approach, we consider that the particle populations are cooled mainly by synchrotron emission, and thus characterized by a spectral break of 1. The data in the optical and X-ray bands are used to constrain the index of the electron population  $\alpha_{e,2}$ , which is then used to derive  $\alpha_{e,1}$  and  $\alpha_{p,1,2}$ .

The value of  $\gamma_{p,min}$  does not affect the modelling as long as it is low enough, so it can be considered as a fixed parameter. It impacts however the value of the particle energy density in the emitting region (especially if the proton-distribution slope is softer than 2.0). To be conservative, and in order not to bias our solutions by a systematic reduction of the total proton energy density, we fix it at  $\gamma_{p,min} = 1$ .

The value of  $\gamma_{p,max}$  is constrained by physical considerations on acceleration and cooling time-scales. In particular, assuming that the acceleration takes place at diffusive shocks, the expression of the acceleration time-scale (see e.g. Drury 1983; Protheroe & Clay 2004; Rieger et al. 2007) can be expressed as

$$\tau_{acc} = \frac{1}{\psi} \frac{m_p c}{e B} \gamma_p \quad (17)$$

where  $\psi$  is an efficiency factor characterizing the acceleration rate, and has been fixed at a physically plausible value of 1/10 (see M01). The cooling terms are represented by the adiabatic losses ( $\tau_{ad} = 2 R/c$ ), the synchrotron losses (the inverse of the synchrotron cooling rate, see Equation 15) and the photo-meson losses (expressed analytically following Sikora et al. 2009). The maximum proton energy depends on the most rapid cooling mechanism. It is determined from the equality  $\tau_{acc}(\gamma_{p,max}) = \min[\tau_{ad}; \tau_{syn}(\gamma_{p,max}); \tau_{pm}(\gamma_{p,max})]$  with  $\tau_{syn}$  and  $\tau_{pm}$  the characteristic time-scales for synchrotron and photo-meson losses, respectively.

The plot on the right panel of Fig. 1 shows an example of all the relevant time-scales in the emitting region. Under the assumption that the photo-meson losses are always the slowest, which holds for the application to AGN without strong external photon fields discussed in the present paper, we have to consider two different regimes,  $\tau_{ad} \leq \tau_{syn}$  or  $\tau_{ad} > \tau_{syn}$ , for all  $\gamma \leq \gamma_{p,max}$ .

#### 2.3.1 Adiabatic cooling dominated regime ( $\tau_{ad} \leq \tau_{syn}$ )

In this regime, the fastest cooling mechanism for all  $\gamma_p \leq \gamma_{p,max}$  is the adiabatic one, and no break is expected in the proton energy distribution. The equation  $\tau_{acc}(\gamma_{p,max}) = \tau_{ad}$  is thus used to define  $\gamma_{p,max}$ :

$$\gamma_{p,max} = 6.44 \times 10^9 \frac{B}{1G} \frac{R}{10^{17}cm} \quad (18)$$

The condition on the cooling terms translates into a relation between the size of the emitting region and the magnetic field:

$$\frac{R}{10^{17}cm} \leq 10.13 \frac{B}{1G}^{-3/2} \quad (19)$$

The peak frequency of the proton synchrotron component can be derived from the synchrotron emissivity and the expression (Equation 18) for  $\gamma_{p,max}$  as (see e.g. Tavecchio et al. 1998; Cerruti et al. 2013a):

$$\frac{\nu_{peak,p}}{10^{27}Hz} = \frac{1.25 \times 10^{-3}}{1+z} \frac{(3 - \alpha_{p,1})}{1.5} \frac{\delta}{10} \left( \frac{B}{1G} \right)^3 \left( \frac{R}{10^{17}cm} \right)^2 \quad (20)$$

where  $z$  is the redshift of the source and the numerical coefficient takes into account the exponential cut-off at  $\gamma_{p,max}$ . Interestingly, considering Equation 19,  $\nu_{peak,p}$  has to be lower than a given value which is a function only of the injection index  $\alpha_{p,1}$  and the Doppler factor:

$$\frac{\nu_{peak,p}}{10^{27}Hz} \leq \frac{0.128}{1+z} \frac{(3 - \alpha_{p,1})}{1.5} \frac{\delta}{10} \quad (21)$$

or, in terms of the peak energy,

$$\frac{E_{peak,p}}{1TeV} \leq \frac{0.529}{1+z} \frac{(3 - \alpha_{p,1})}{1.5} \frac{\delta}{10} \quad (22)$$

This inequality shows the capability of hadronic models to reproduce the observed peak of the UHBL  $\gamma$ -ray emission at TeV energies.

An additional constraint comes from the observed variability time-scale  $\tau_{var}$  and the usual causality argument:

$$\frac{R}{10^{17}cm} \leq \frac{2.59}{1+z} \frac{\delta}{10} \frac{\tau_{var}}{10 \text{ days}} \quad (23)$$

We can thus systematically study the parameter space for a given value of  $\delta$  by iterating over  $R$ , starting from the maximum allowed value, (Equation 23), and over  $B$ , which is constrained by Equation 20, while keeping the value of  $\nu_{peak,p}$  consistent with the data. The value of  $\gamma_{p,max}$  is then computed following Equation 18. The luminosity of the high-energy component of the SED fixes the normalization of the proton distribution (the parameter  $\eta = K_p/K_e$ ), which is the last free parameter of the hadronic component.

Now turning to the leptonic component, the break in the electron distribution is fixed by the equality of the adiabatic and the synchrotron time-scale ( $\tau_{ad} = \tau_{syn}(\gamma_{e,break})$ ), and can be expressed as:

$$\gamma_{e,break} = 75 \left( \frac{B}{1G} \right)^{-2} \left( \frac{R}{10^{17}cm} \right)^{-1} \quad (24)$$

As can be seen, in the proton-synchrotron scenario (characterised by  $B \gtrsim 1$  G) the magnetic field is sufficiently high such that the entire leptonic population is cooled by synchrotron emission and is thus described by a simple power-law function with index  $\alpha_{e,2} = \alpha_{p,1} + 1$ .

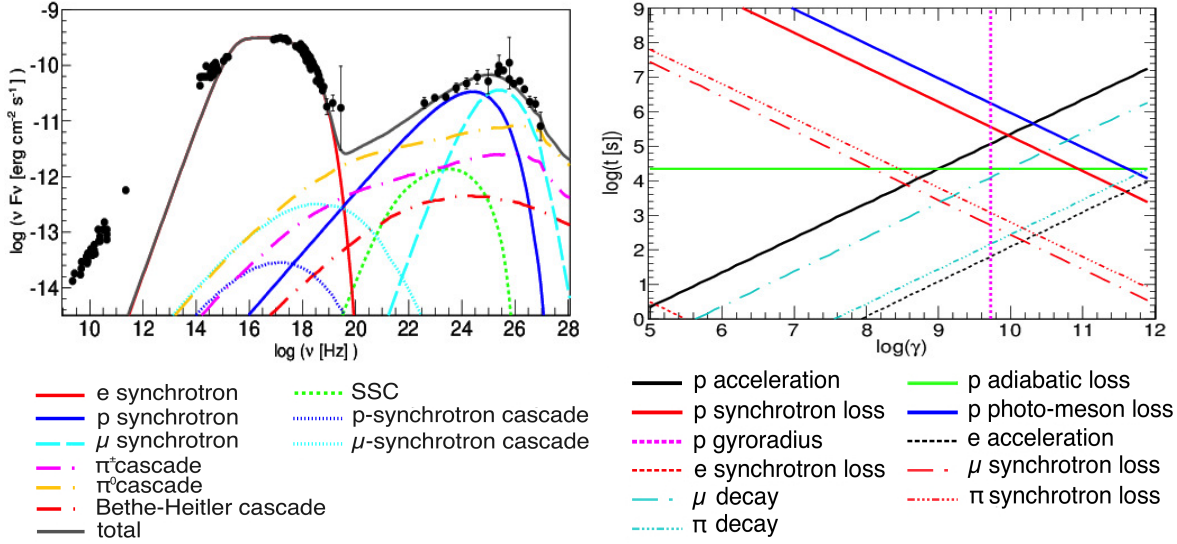


**Figure 1.** *Left:* hadronic modeling of the spectral energy distribution of Mrk 421 (data points taken from Abdo et al. 2011). Data have been corrected for the EBL absorption, which is thus not included in the model. *Right:* acceleration and cooling time-scales for the different particles in the emitting region. For the parameter values, see Section 3.

The remaining free parameters are the normalization of the electron distribution, which is constrained by the luminosity of the low-energy component of the SED, and the maximum energy of the electrons  $\gamma_{e,\text{max}}$ . In our model, the latter is constrained by the observed peak of the low-energy bump in the SED (and not by the equality of the acceleration and cooling time-scales, as discussed in Section 5):

$$\gamma_{e,\text{max}} = 1.64 \times 10^5 (1+z) \left( \frac{\nu_{\text{peak},e}}{10^{18} \text{Hz}} \right)^{1/2} \left( \frac{\delta}{10} \right)^{-1/2} \left( \frac{B}{\text{IG}} \right)^{-1/2} \quad (25)$$

### 2.3.2 Synchrotron cooling dominated regime ( $\tau_{ad} > \tau_{\text{syn}}$ )

In this second regime, the synchrotron cooling time-scale is shorter than the adiabatic one for all  $\gamma_p \leq \gamma_{p,\text{max}}$ . The first consequence is that the stationary proton distribution is described by a broken power-law, with index  $\alpha_{p,2} = 1 + \alpha_{p,1}$  above  $\gamma_{p,\text{break}}$ . The maximum proton energy is determined by the equation  $\tau_{\text{acc}}(\gamma_{p,\text{max}}) = \tau_{\text{syn}}(\gamma_{p,\text{max}})$ , which yields:

$$\gamma_{p,\text{max}} = 6.53 \times 10^{10} \left( \frac{B}{\text{IG}} \right)^{-1/2} \quad (26)$$

The relation  $\tau_{ad} = \tau_{\text{syn}}(\gamma_{p,\text{break}})$  is used to define the proton break energy:

$$\gamma_{p,\text{break}} = 6.61 \times 10^{11} \left( \frac{B}{\text{IG}} \right)^{-2} \left( \frac{R}{10^{17} \text{cm}} \right)^{-1} \quad (27)$$

In this case we expect  $\gamma_{p,\text{break}} < \gamma_{p,\text{max}}$ , and indeed this inequality leads to

$$\frac{R}{10^{17} \text{cm}} > 10.13 \frac{B}{\text{IG}}^{-3/2} \quad (28)$$

which is complementary to Eq. 19, as expected.

The peak frequency of the proton synchrotron component is associated to  $\gamma_{p,\text{break}}$  only if  $\alpha_{p,1} \in (2.0, 3.0)$ . In this case,

$$\frac{\nu_{\text{peak},p}}{10^{27} \text{Hz}} = \frac{13.15 (3 - \alpha_{p,1})}{1+z} \frac{\delta}{1.5} \frac{1}{10} \left( \frac{B}{\text{IG}} \right)^{-3} \left( \frac{R}{10^{17} \text{cm}} \right)^{-2} \quad (29)$$

By imposing the condition from Equation 28, we find again that the

upper bound for  $\nu_{\text{peak},p}$  is given by the inequality in Equation 21. On the other hand, if  $\alpha_{p,1} < 2.0$ , the peak frequency is associated with  $\gamma_{p,\text{max}}$ . In this case  $\nu_{\text{peak},p}$  is constant, and equal to

$$\frac{\nu_{\text{peak},p}}{10^{27} \text{Hz}} = \frac{0.128 (3 - \alpha_{p,2})}{1+z} \frac{\delta}{1.5} \frac{1}{10} \quad (30)$$

which is a factor  $1 - 1/(3 - \alpha_{p,1})$  lower than the one in Equation 21. There exists thus a maximum peak frequency of the proton synchrotron emission, corresponding to the equality in Equation 21, for which  $R$  and  $B$  are related via the equality in Equations 19 and 28. This is the case where  $\tau_{\text{acc}}(\gamma_{p,\text{max}}) = \tau_{ad} = \tau_{\text{syn}}(\gamma_{p,\text{max}})$ .

For a given value of  $\delta$ , we can again study systematically the parameter space, iterating over  $R$  and  $B$ , with  $\nu_{\text{peak},p}$  constrained by the data. Here, we are applying again the constraint on  $\tau_{\text{var}}$  (Equation 23) and the constraints on the electron distribution (Equations 24 and 25), though generally, in this regime,  $\gamma_{e,\text{break}}$  occurs below or very close to  $\gamma_{e,\text{min}}$ .

### 2.3.3 Additional constraints

One may think that another constraint on the maximum energy of protons in the emitting region could be provided by their gyro-radii in the assumed homogeneous magnetic field: particles with gyro-radius larger than  $R$  would escape the emitting region, and should not be considered in the framework of a stationary emission model. For relativistic particles, the expression of the gyro-radius is

$$R_{\text{gyro}} = \frac{m c^2}{e B} \gamma \quad (31)$$

However, for the protons in the emitting region, by substituting the values of  $\gamma_{p,\text{max}}$  in Equation 31, it is easy to show that  $R_{\text{gyro}}$  is always smaller than  $R$ , i.e. even the most energetic protons are confined in the plasma blob, given the constraints from acceleration and loss time-scales.

For a given Doppler factor  $\delta$ , the equations described above can be used to determine the complete set of solutions for a proton-synchrotron scenario by systematically scanning different values of

the magnetic field  $B$  and the size of the emission region  $R$ . This scenario provides a satisfactory description of the blazar SED only for values of  $\nu_{peak,p}$  in agreement with the observed peak frequency of the high-energy bump in the SED. Removing this constraint on  $\nu_{peak,p}$ , and studying the parameter space for all other values of  $R$  and  $B$ , we discovered an interesting part of the parameter space, in which  $B$  is too low for a dominant proton-synchrotron component and the denser emission region leads to a significant contribution from secondary pairs from p- $\gamma$  interactions. This set of secondary solutions exists only in the regime where  $\tau_{ad} \leq \tau_{syn}$ , and is systematically studied by iterating over  $R$  and  $B$  for lower values of  $\nu_{peak,p}$  (see Equation 20) and normalizing the secondary-pair synchrotron emission in order to match the observed gamma-ray emission. The resulting lepto-hadronic scenario is very distinct from the proton-synchrotron scenario and resembles more the “proton-induced cascade” model by Mannheim (1993).

In this lepto-hadronic scenario, the primary leptonic population is not completely cooled down by synchrotron emission, and a cooling break should be present in their stationary distribution. In this case, the electron particle population is thus defined by a broken power-law with  $\alpha_{e;1} = \alpha_{p;1}$ ,  $\alpha_{e;2} = \alpha_{e;1} + 1$ , and  $\gamma_{e;break}$  is given by Equation 24.

The lepto-hadronic solutions occupy a region in the parameter space with low  $B$  ( $\sim 0.1$  to a few G) and higher particle densities than in the proton-synchrotron solutions. In this scenario, proton synchrotron radiation can lead to a small spectral bump at intermediate energies between the X-ray and *Fermi*-LAT bands and the primary proton spectrum is not significantly cooled. Both SSC emission and photons from proton-induced cascades contribute to the high-energy bump.

### 3 APPLICATION TO Mrk 421

As a first application of our code we have studied the SED of the well known HBL Mrk 421, which was the very first extragalactic source detected at TeV energies (Punch et al. 1992). Its VHE spectrum has been well studied with the current generation of Cherenkov telescopes (Aharonian et al. 2005; Albert et al. 2007; Acciari et al. 2009). Up to now, the most complete simultaneous SED of Mrk 421 in a low state has been published by Abdo et al. (2011), including data from *Fermi*-LAT and *MAGIC*. Apart from the usual SSC model, the authors applied also a hadronic model to this SED, using the code by M01. We have applied our code to this data set to compare the result with an existing model.

The low-energy component of the SED can be satisfactorily associated with a completely cooled leptonic population with power-law index  $\alpha_{e;2} = 2.9$  and a simple exponential cut-off. Following the physical constraints presented in Section 2, we impose thus  $\alpha_{p;1} = 1.9$ . To compare our model directly with the one presented in Abdo et al. (2011), we adopt the same value for the magnetic field,  $B = 50$  G. The main difference with respect to their model comes from the constraint on  $\gamma_{p;max}$  and, in particular, from the hypothesis on the acceleration mechanism (equation 17). M01 considered a more efficient acceleration term due to oblique shocks, yielding higher values for  $\gamma_{p;max}$ . To compensate for this effect we use a higher Doppler factor (25 instead of 12). We find a similar solution imposing  $\nu_{peak,p} = 3 \times 10^{24}$  Hz in equation 20, which results in  $R = 3.3 \times 10^{14}$  cm and  $\gamma_{p;max} = 1.06 \times 10^9$  (compared respectively to  $4 \times 10^{14}$  cm and  $2.3 \times 10^9$  in Abdo et al. 2011). In Figure 1 we present the results

object	$\sigma$	$\Gamma$	$\Phi_0$	$E_{dec}$	$E_{max}$
1ES 0229+200	9.1	$1.90 \pm 0.16$	$1.67 \pm 0.31$	5.03	171
1ES 0347-121	6.8	$1.70 \pm 0.14$	$1.09 \pm 0.25$	5.16	27
RGB J0710+591	16.4	$1.56 \pm 0.09$	$1.45 \pm 0.18$	7.24	175
1ES 1101-232	9.4	$1.91 \pm 0.16$	$3.60 \pm 0.62$	3.50	48
1ES 1218+304	42.0	$1.68 \pm 0.03$	$17.16 \pm 0.87$	4.48	366

**Table 2.** Results from the analysis of *Fermi*-LAT data. For all objects the best-fit model is given by a power-law function with index  $\Gamma$ . The differential flux normalization  $\Phi_0$  is in units of ( $10^{-14}$  cm $^{-2}$  s $^{-1}$  MeV $^{-1}$ ), and computed at the decorrelation energy  $E_{dec}$  (in GeV). We also provide the energy ( $E_{max}$ , in GeV) of the most energetic photon consistent with the source position. The significance of the detection is expressed in standard deviations ( $\sigma$ ) above the background.

of the modeling: the high energy bump of the SED is ascribed to different components, with the muon synchrotron emission dominating the VHE emission, and cascades dominating above  $10^{27}$  Hz. This example illustrates the importance of a detailed simulation of secondary particles from p- $\gamma$  interactions. It can also be seen that synchrotron emission from muons cannot be neglected.

Besides the small differences in the parameter values imposed by our physical constraints, our code fully reproduces the result presented in Abdo et al. (2011). In addition we are able to correctly estimate the emission by the cascades triggered by Bethe-Heitler pair production, which is negligible with respect to the emission by cascades associated with the photo-meson interaction. Although negligible in this case, as we show later, the SSC component can play an important role in the lepto-hadronic scenario. It should be noted that for this first application, we have not carried out a systematic scan of the parameter space, as will be done for the investigation of the UHBLs in the following section.

### 4 MODELLING OF ULTRA-HIGH-FREQUENCY-PEAKED BL LACS

We have modelled the SEDs of the five UHBLs listed in Table 1 with our code in a systematic way. The model parameters have been constrained following the relations detailed in Section 2.3. For a given value of the Doppler factor (fixed in the following at  $\delta = 30$ ), we scan the parameter space in  $R$  and  $B$ , while the remaining free parameters are all determined by physical assumptions and by observations. The maximum value of  $R$  is determined from equation 23 by assuming  $\tau_{var} = 10$  days, except for the modelling of 1ES 1218+304, for which a variability time-scale of one day has been adopted, based on observational evidence (Acciari et al. 2010a). Under the assumption that leptons and protons emitting at all energies are confined in the same emitting region,  $\tau_{var}$  should be considered as the shortest variability time-scale at all wavelengths. Beside 1ES 1218+304, for 1ES 0229+200 (Aliu et al. 2014) and RGB J0710+591<sup>4</sup> a  $\tau_{var}$  of the order of ten days has been observed in soft X-rays. Regardless of the exact value of  $\tau_{var}$ , radii larger than  $10^{18}$  cm can also be excluded on the basis of the required

<sup>4</sup> See <http://www.swift.psu.edu/monitoring/source.php?source=RGBJ0710+591>



power of the emitting region (see Fig. 2 and Section 5), as well as the opening angle of relativistic jets measured in the radio band. For all sources we have arbitrarily imposed a minimum size of the emitting region  $R_{min} = 10^{14-15}$  cm, which corresponds to  $\sim 10$  gravitational radii for a SMBH of  $10^{8-9} M_{\odot}$  (see Table 1 for the exact value of  $M_{\bullet}$  we considered). This is based on the expectation that the size of the emitting region will likely be at least of order the scale of the base of the jet.

Multi-wavelength data have been taken from Aliu et al. (2014, for 1ES 0229+200); Aharonian et al. (2007b, for 1ES 0347-121); Acciari et al. (2010b, for RGB J0710+591); Aharonian et al. (2007a, Fig.6, upper panel, for 1ES 1101-232); and R ger et al. (2010, for 1ES 1218+304). In this work, publicly available data from the *Fermi*-LAT taken from August 4, 2008 to February 15, 2014 (MJD 54682-56703) were analyzed using the standard *Fermi* analysis software, version v9r32p5, available from the Fermi Science Support Center (FSSC)<sup>5</sup>. Events with energy between 100 MeV and 500 GeV were selected from the Pass 7 data set. Only events passing the SOURCE class filter and located within a square region of side length  $20^{\circ}$  centered on the source position were selected. Cuts on the zenith angle ( $< 100^{\circ}$ ) and rocking angle ( $< 52^{\circ}$ ) were applied to the data. The post-launch *P7SOURCE\_V15* instrument response functions (IRFs) were used in combination with the corresponding Galactic and isotropic diffuse emission models. The model of the region includes the diffuse components and all sources listed in the Second Fermi-LAT Catalog (2FGL Nolan et al. 2012) located within a  $20^{\circ}$  circle centered on the source. The spectral parameters of the sources were left free during the fitting procedure. A power-law correction in energy with free normalization and spectral slope was applied to the Galactic diffuse component. Events were analyzed using the binned maximum likelihood method as implemented in *glike*. The results of our *Fermi*-LAT analysis are shown in Table 2.

Among the five sources under study, only RGB J0710+591, 1ES 1101-232, and 1ES 1218+304 are included in the 2FGL catalog. Our analysis is fully consistent with the 2FGL for both 1ES 1101-232 and 1ES 1218+304, while for RGB J0710+591 only the spectral index is consistent but not the flux normalization (the differential flux from the 2FGL, estimated at the same energy provided in Table 2, is  $(2.26 \pm 0.34) \times 10^{-14} \text{ cm}^{-2} \text{ s}^{-1} \text{ MeV}^{-1}$ ). This discrepancy may be due to the known variability of the source at GeV energies<sup>6</sup>.

The GeV emission from 1ES 0229+200 was first studied by Dermer et al. (2011), who analyzed LAT data from August 2008 to September 2010 without detecting the source. With a larger data-set (3.25 years of *Fermi*-LAT observations), and considering only energies from 1 to 300 GeV, Vovk et al. (2012) have claimed the first GeV detection of the source. They estimated a 1 – 300 GeV spectral index of  $1.36 \pm 0.25$  and a flux normalization of  $(2.15 \pm 1.45) \times 10^{-15} \text{ cm}^{-2} \text{ s}^{-1} \text{ MeV}^{-1}$  at our decorrelation energy. The discrepancy in the spectral index estimation between our work and the results presented by Vovk et al. (2012) could be related both to the different energy band in which the fit was performed, as well as the different time range. In order to perform a better comparison, we analyzed the same time interval analyzed by Vovk

et al. (2012), but using all the *Fermi*-LAT photons from 100 MeV to 500 GeV. The resulting index is  $2.14 \pm 0.19$ , with a differential flux of  $(4.80 \pm 1.25) \times 10^{-14} \text{ cm}^{-2} \text{ s}^{-1} \text{ MeV}^{-1}$  at  $E_0 = 2.69 \text{ GeV}$ , consistent with the results from the 2008-2014 analysis, but again not in agreement with the results from Vovk et al. (2012).

The remaining possibility is that the discrepancy is due to the different energy band used for the fit, indicating a spectral softening at MeV energies. The catalog of *Fermi* sources above 10 GeV (1FHL, Ackermann et al. 2013a) differs indeed from the results included in the 2FGL. Alternatively, the difference could be related to contamination from the Milky Way foreground which dominates at lower energies, as discussed for example in H.E.S.S. Collaboration et al. (2012).

For 1ES 0347-121 our result agrees with the *Fermi*-LAT analysis recently presented by Tanaka et al. (2014).

In the following, we include these new *Fermi*-LAT spectra in our SEDs, with the exception of RGB J0710+591, for which, given the GeV variability, we used the spectrum estimated by (Acciari et al. 2010b) that is simultaneous with the *VERITAS* observations.

For the five sources, we find two distinct sets of solutions, corresponding to the proton-synchrotron scenario and a lepto-hadronic scenario, dominated by emission from secondary particles from p- $\gamma$  interactions. In the latter case, the SSC contribution is at a level comparable to the emission from hadronic processes, and justifies the “lepto-hadronic” classification. When scanning the parameter space, we compute for each model curve the  $\chi^2$  deviation with respect to the observational data. This information is used to determine the solution which provides the best description of the SED, as well as the 1- $\sigma$  region in the *B-R* plane (which corresponds to  $\Delta\chi^2 \leq 2.3$ , i.e. to a significance of  $1\sigma$  for two free parameters). The evaluation of the  $\chi^2$  ranges was done separately for the two sets of solutions. Given the degeneracy of the problem and the difficulty in accounting correctly for different statistical and systematic uncertainties between the data sets, an actual  $\chi^2$  minimisation was not attempted.

In the top panel of Figure 2 we show the two families of solutions for the case of RGB J0710+591, which is the only source for which there is a *Fermi*-LAT spectrum simultaneous with VHE observations. The corresponding plots for the other four sources are provided in Appendix A (Figure A1 for 1ES 0229+200, Figure A2 for 1ES 0347-121, Figure A3 for 1ES 1101-232, and Figure A4 for 1ES 1218+304).

The location of the two solutions in the parameter space is represented in the bottom panel of Figure 2, in which we show the contour-plot in the *B-R* plane, as well as the ratio between the particle and magnetic energy density versus the total kinetic plus magnetic power of the emitting material. The total power of the emitting region is evaluated as

$$L = \pi R^2 c \Gamma_{bulk}^2 (u_B + u_e + u_p) \quad (32)$$

where  $\Gamma_{bulk} = \delta/2$ , and  $u_B$ ,  $u_e$  and  $u_p$  represent the energy densities of the magnetic field, the electrons, and the protons, respectively. The resulting ranges of all the parameter values are reported in Tables 3 and 4 for the five sources and for each of the two scenarios. It can be seen from Figure 2 that the “proton-synchrotron” solutions consist principally of the electron-synchrotron component at low energies and the proton-synchrotron component at high energies. Only very small contributions from proton-synchrotron induced cascades and from muon-synchrotron emission are visible at low and high energies, respectively. For this scenario, the synchrotron-

<sup>5</sup> <http://fermi.gsfc.nasa.gov/ssc/>

<sup>6</sup> See [http://tevcat.uchicago.edu/LATCat2/spectra/lat\\_1281.html](http://tevcat.uchicago.edu/LATCat2/spectra/lat_1281.html).

cooling-dominated regime is accessible for all the sources but RGB J0710+591, the only source for which we used simultaneous *Fermi*-LAT measurements to constrain the models.

In the lepto-hadronic solutions, the low-energy bump is still due to electron-synchrotron emission, while the high-energy bump is a combination of SSC and pion-induced cascade emission. The proton-synchrotron component is strongly suppressed and shifted to intermediate energies.

As can be seen in the SED plots, our models do not always describe the available data on the MeV-GeV emission correctly. While the results for 1ES 0229+200 and RGB J0710+591 match the *Fermi*-LAT measurements (even though for 1ES 0229+200 the proton-synchrotron model systematically underestimates the data at  $\approx 100$  MeV), for the other three sources our models can reproduce either the spectral index, or the normalization, but not both of them. In general, the lepto-hadronic solutions predict flatter GeV spectra, more in agreement for example with the *Fermi*-LAT spectrum of 1ES 1101-232.

This inconsistency may well be attributable to the long term  $\gamma$ -ray variability of the five UHBLs (as suggested for 1ES 0229+200 by VERITAS, see Aliu et al. 2014): the *Fermi*-LAT bow-ties are estimations of the average  $\gamma$ -ray emission integrated over five years. Looking at the SEDs of 1ES 1101-232 and 1ES 1218+304, it is clear that there is indeed some conflict between the *Fermi* and the IACT measurements at  $\approx 100$  GeV.

The *Fermi*-LAT measurements should thus be considered as an estimation of the mean MeV-GeV emission, and not used to put strong constraints on the models. The exception is RGB J0710+591, for which we used the strictly simultaneous *Fermi* data provided by Acciari et al. (2010b). In this case our models correctly reproduce the *Fermi*-LAT flux and spectral index. We conclude that the mismatch between our model and the average *Fermi* spectra might well be due to long- or medium-term variability of the source spectra.

## 5 DISCUSSION

Lepto-hadronic modelling can reproduce well the VHE emission of the UHBLs under study, as well as the lower energy SEDs (with the caveat on the non-simultaneous *Fermi*-LAT data discussed in the previous Section). Compared to standard leptonic models, our solutions have the advantage of avoiding large values of the Doppler factor of the emitting region. The minimum Lorentz factor of the electron population  $\gamma_{e,min}$  is of the order of  $10^{2-3}$  or smaller in the proton-synchrotron scenario, in line with the values required in leptonic modelling of common HBLs. For the lepto-hadronic solutions,  $\gamma_{e,min}$  can be as low as 1 (for 1ES 0229+200 and RGB J0710+591), while it is of the order of  $10^{3-4}$  for the other sources, due to constraints from the optical data. Only 1ES 1101-232 requires a  $\gamma_{e,min}$  of  $10^4$  for all lepto-hadronic solutions.

On the other hand, the only parameter that takes particularly non-trivial values for all our solutions is the spectral index of the particle population: for all sources, we need very hard injection functions ( $\alpha_{p,1} = \alpha_{e,1} \in [1.3 - 1.5]$ ). Such hard spectra are at odds with the simplest diffusive shock acceleration models, which predict injection indices close to 2.0 (see e.g. Drury 1983; Bednarz & Ostrowski 1998; Achterberg et al. 2001; Protheroe & Clay 2004; Rieger et al. 2007). A particle index of 1.5 is usually considered as the lower limit still in agreement with simple acceleration scenarios (see Aharonian et al. 2006). However, harder values

(even lower than 1.5) are still possible in certain acceleration scenarios (see Ellison et al. 1990; Vainio et al. 2003). Second-order Fermi acceleration may also produce hard ( $\alpha < 1.5$ ) spectra (see Virtanen & Vainio 2005). Another mechanism for efficiently accelerating particles is magnetic reconnection; in this case as well it is possible to obtain hard ( $\alpha \approx 1.5$ ) particle energy distributions (see e.g. Cerutti et al. 2012; Sironi & Spitkovsky 2014).

It should be stressed, however, that low values of  $\alpha_{e,1}$  and  $\alpha_{p,1}$  are not directly constrained by observations and come from two physical assumptions detailed in Section 2.3: (i) the hypothesis that the leptonic particle population is simply cooled by synchrotron emission, and characterised by a break in the spectral index of  $\Delta\Gamma = 1.0$ ; and (ii) the hypothesis that protons and electrons are co-accelerated in magnetic fields with a single power-law spectrum of turbulence over a wide range of scales, sharing the same injection index. Relaxing one or more of these assumptions can allow solutions with  $\alpha_{p,1} \geq 1.5$  and  $\alpha_{e,1} \geq 1.5$ .

In standard SSC modelling of HBLs, a spectral break of 1.0 is rarely observed (Tavecchio et al. 2010; Cerruti et al. 2013a), suggesting that acceleration and cooling in the emitting region is more complicated, with additional injection/escape terms. On the other hand, the magnetic turbulence spectrum may well be appreciably different for scales corresponding to gyroradii of TeV and EeV particles, resulting in  $\alpha_{p,1} \neq \alpha_{e,1}$ .

Values of  $\alpha_{p,1}$  softer than 1.3-1.5 would provide as well a better fit of the *Fermi*-LAT measurements, without affecting significantly the other parameters. In summary, the hard injection spectrum does not represent a limitation of the hadronic model itself, but might point instead to the operation of mechanisms for acceleration and/or cooling beyond the simplest expectations.

The hard particle spectra is also responsible for the difference between the hadronic modelling of UHBLs and the solution shown for Mrk 421 in Section 3 ( $\alpha_{p,1} = 1.9$ ): with larger values of  $\alpha_{p,1}$  the number of p- $\gamma$  interactions increases, and the synchrotron emission from muons and cascades becomes more significant. In addition, the modelling of Mrk 421 used a lower emission region size ( $R = 3.3 \times 10^{14}$  cm) with a higher particle density, which also increases the number of p- $\gamma$  interactions. These two differences explain why we could not find a similar solution, dominated by muon synchrotron emission together with a very significant cascade component in the proton-synchrotron scenario for UHBLs. In the *B-R* contour-plot, larger values of  $\alpha_{p,1}$  would affect the proton-synchrotron parameter space by lowering the maximum value of  $\nu_{peak,p}$  (see Equation 21 and 29) for given values of *R* and *B* and thus shrinking the width of the proton-synchrotron band of solutions. On the other hand, solutions dominated by secondary p- $\gamma$  particles would show up for higher values of  $\nu_{peak,p}$  (i.e. for a larger size and stronger magnetic field, see Equation 20), moving the "island" of lepto-hadronic solutions closer to the proton-synchrotron domain.

The two main arguments generally put forward to disfavour hadronic blazar models are the energy budget of the emitting region and the constraints from short variability time-scales.

The total power of the emitting region (Equation 32) need not necessarily be limited by the Eddington luminosity of the black hole, as is observed to be case for some narrow-line Seyfert 1 galaxies, and especially gamma-ray bursts. Nevertheless, for radio-loud AGN hosted by SMBHs with masses in the range  $10^{8-9} M_{\odot}$ , observational estimates of jet powers generally do not show any

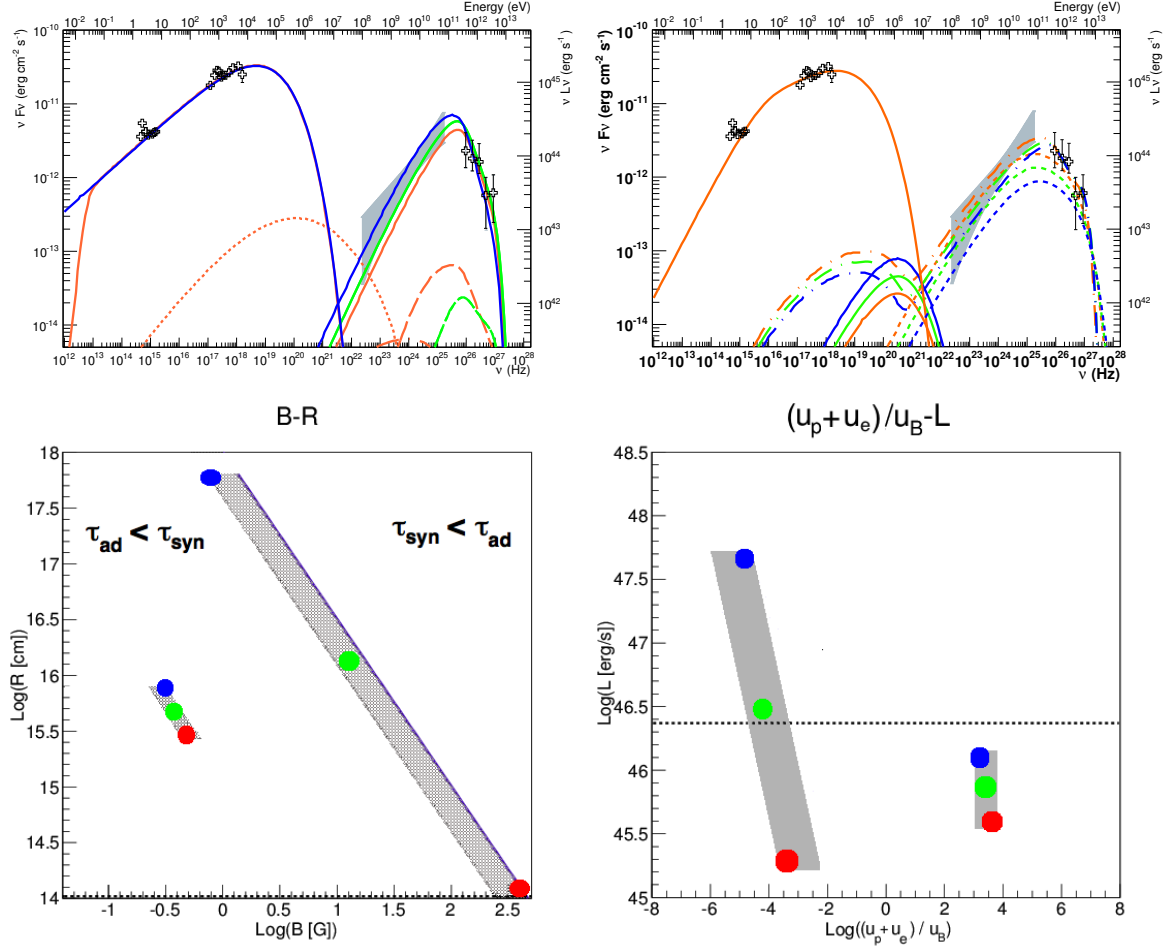


**Figure 2.** *Top:* modelling of the SED of RGB J0710+591, using data from Acciari et al. (2010b). *left:* proton-synchrotron scenario for  $(B[G], R[\text{cm}]) = (1, 6.7 \times 10^{17}), (21, 8.2 \times 10^{15}), (446, 1 \times 10^{14})$ ; *right:* leptohadronic scenario for  $(B[G], R[\text{cm}]) = (0.3, 8 \times 10^{15}), (0.4, 5 \times 10^{15}), (0.6, 3 \times 10^{15})$ . Colours are used to identify the components corresponding to the same exemplary solutions in the  $B$ - $R$  parameter space. In the left plot, from lower to higher energies, the SED components are (with the same line-style as in Fig. 1): electron synchrotron emission (solid lines), synchrotron emission from cascades associated with proton synchrotron emission (dotted lines), proton-synchrotron emission (solid line, high energies) and muon synchrotron emission (dashed lines). In the right plot, the visible components are: electron synchrotron emission (solid line), proton synchrotron emission (solid lines at intermediate energies), SSC emission (dotted lines) and the sum of SSC emission and the synchrotron emission from  $\pi^0$ - and  $\pi^\pm$ -induced cascades (dashed lines). The negligible Bethe-Heitler component has not been computed to save CPU time. For a more detailed view of all the secondary particles associated with  $p$ - $\gamma$  interactions, see Figure 1. *Bottom left:* representation in the  $B$ - $R$  plane of the two distinct regions of solutions. The solid violet line corresponds to the equality in Equations 19, and the nearby shadowed region represents the band of acceptable parameters for the proton-synchrotron scenario. The separate set of solutions in the bottom-left part of the plot represents the leptohadronic scenario. Solutions with  $R \leq 10^{14}$  cm have been excluded. The three coloured dots correspond to the solutions shown in the top plots. *Bottom right:* same as the previous plot, but in the  $(u_p + u_e)/u_B$  -  $L$  plane. The horizontal dotted line represents the Eddington limit for  $M_\bullet = 10^{8.25} M_\odot$ .

evidence for highly super-Eddington values (e.g. Cavagnolo et al. 2010). The Eddington luminosity for RGB J0710+591 (using the SMBH mass estimate provided in Table 1), is denoted with a dotted line in the bottom-right plot of Fig. 2, as well as in Appendix A for all the other sources. As can be seen, our solutions are all characterised by  $\log(L) \in [45, 48]$ . While the solutions with the highest luminosities (i.e. lowest magnetic field and largest size) may be disfavored, a significant part of the hadronic solutions do not exceed the Eddington value. However, note that for the two UHBLs with the lowest SMBH mass estimates (1ES 0347-121 and 1ES 1218+304), the total luminosity for the leptohadronic models becomes comparable with the Eddington luminosity of the SMBH.

The relatively low luminosities of our leptohadronic solutions are

also related to the hard proton spectra: for  $\alpha_{1;p} < 2.0$  the proton energy density is dominated by hadrons at  $\gamma_{p,max}$ . On the other hand, if  $\alpha_{1;p} \geq 2.0$  the contribution of the low-energy part of the proton distribution becomes dominant in the evaluation of  $u_p$ , and thus  $L$ . Softer injection spectra, although more in agreement with simple shock acceleration scenarios, would thus have the disadvantage of significantly increasing the total power of our solutions.

The energy budget of the emitting region is dominated by the magnetic field energy density  $u_B$  for the proton-synchrotron scenario, and by the proton energy density  $u_p$  in the leptohadronic scenario. The equipartition factor  $(u_p + u_e)/u_B$  (which is  $\approx u_p/u_B$ ) is provided for all the sources in Tables 3 and 4. Equipartition is often used to reduce the number of free parameters in blazar modelling, pro-

**Table 3.** Parameters used for the hadronic modelling of our sources (proton-synchrotron scenario)

	1ES 0229+200	1ES 0347-121	RGB J0710+591	1ES 1101-232	1ES 1218+304
$z$	0.140	0.188	0.125	0.186	0.184
$\delta$	30	30	30	30	30
$R_{src}$ [ $10^{16}$ cm]	0.1 – 68	0.03 – 65	0.01 – 67	0.1 – 66	0.03 – 6.6
$B$ [G]	1.0 – 160	1.0 – 296	1.0 – 446	1.0 – 133	3.4 – 454
$*u_B$ [erg cm $^{-3}$ ]	0.04 – 1017	0.04 – 3480	0.04 – 7900	0.04 – 704	0.5 – 8210
$\gamma_{e,min}$ [ $10^2$ ]	1.6 – 20	2.2 – 38	0.01	4.3 – 50	2.3 – 27
$\gamma_{e,break}$ [ $10^3$ ]	$\leq \gamma_{e,min}$	$\leq \gamma_{e,min}$	0.001 – 0.03	$\leq \gamma_{e,min}$	$\leq \gamma_{e,min}$
$\gamma_{e,max}$ [ $10^5$ ]	0.3 – 4.1	0.1 – 2.1	0.2 – 3.7	0.07 – 0.8	0.04 – 0.5
$\alpha_{e,1} = \alpha_{p,1}$	1.3	1.7	1.35	1.7	1.7
$\alpha_{e,2} = \alpha_{p,2}$	2.3	2.7	2.35	2.7	2.7
$K_e$ [cm $^{-3}$ ]	$7.0 \times 10^{-8} - 0.36$	$0.05 - 1.2 \times 10^5$	$7.3 \times 10^{-5} - 1040$	$0.3 - 7.2 \times 10^4$	$3.2 \times 10^{-3} - 8.0 \times 10^4$
$*u_e$ [erg cm $^{-3}$ ]	$2.2 \times 10^{-11} - 3.2 \times 10^{-5}$	$5.7 \times 10^{-7} - 0.7$	$1.6 \times 10^{-9} - 2.8 \times 10^{-2}$	$2.6 \times 10^{-6} - 0.4$	$2.6 \times 10^{-8} - 0.4$
$\gamma_{p,min}$	1	1	1	1	1
$\gamma_{p,break}$ [ $10^9$ ]	2.6 – 57	2.4 – 56	2.8 – 47	3.7 – 56	1.0 – 26
$\gamma_{p,max}$ [ $10^9$ ]	4.8 – 57	3.2 – 56	2.8 – 47	4.8 – 56	3.1 – 26
$\eta$	$(9.7 - 19) \times 10^{-6}$	$(0.7 - 18) \times 10^{-6}$	$(1.0 - 3.3) \times 10^{-7}$	$(0.2 - 2.6) \times 10^{-6}$	$2.1 \times 10^{-6} - 0.02$
$*u_p$ [erg cm $^{-3}$ ]	$6.1 \times 10^{-8} - 0.08$	$4.9 \times 10^{-7} - 4.8$	$3.0 \times 10^{-7} - 6.4$	$5.4 \times 10^{-7} - 0.5$	$5.9 \times 10^{-5} - 3.5$
$*(u_p + u_e)/u_B$ [ $10^{-5}$ ]	0.04 – 36	0.8 – 540	0.3 – 200	2.5 – 430	$0.9 - 2.2 \times 10^3$
$*L$ [ $10^{45}$ erg s $^{-1}$ ]	4.6 – 1670	2.1 – 1120	1.7 – 460	4.6 – 1120	2.6 – 610
$*min(\tau_{ad}; \tau_{syn}(\gamma_{p,max}))$ [hr]	$12 - 1.2 \times 10^4$	$4.3 - 1.2 \times 10^4$	$1.9 - 1.2 \times 10^4$	$19 - 1.2 \times 10^4$	$1.9 - 1.2 \times 10^3$

The luminosity of the emitting region has been calculated as  $L = \pi R^2 c \Gamma_{bulk}^2 (u_B + u_e + u_p)$ , where  $\Gamma_{bulk} = \delta/2$ . In the last row we indicate the time-scale (in hours) which constrains  $\gamma_{p,max}$ , see Section 2.3. If the value of  $\gamma_{e,min}$  required by the modelling is higher than the value of  $\gamma_{e,break}$  estimated from synchrotron cooling, we do not report the value of the latter. The quantities flagged with a star are derived quantities and not model parameters.

viding a specific solution characterised by an equipartition factor close to unity. An equipartition scenario is appealing in particular because it provides the minimum power of the emitting region, and has been successfully applied in leptonic blazar modelling, when adding additional external photon fields (see e.g. Dermer et al. 2014). None of our models is close to equipartition: the best cases are  $(u_p + u_e)/u_B \simeq 0.02$  and  $\simeq 100$  for the proton synchrotron and the lepto-hadronic scenario, respectively. However, this is also the case for widely discussed SSC models for HBLs (see e.g. Cerruti et al. 2013a).

Concerning variability, hadronic models are often disfavored when rapid flares are detected, in view of the typically long cooling times expected for the parent protons (see however Barkov et al. 2012). For the proton-synchrotron and the lepto-hadronic scenarios the associated variability time-scales (at VHE) are respectively the proton synchrotron cooling or the development of synchrotron-pair cascades, which depends on the time-scale of proton-photon interactions. The fastest variability time-scale may be achieved for the proton-synchrotron solutions with the highest  $B$  value: in this case we can have variability of the order of hours in the source frame. In general we have however time-scales of the order of days, which cannot account for minute-long flares, as shown by Aharonian et al. (2007c) or Arlen et al. (2013). With the exception of 1ES 1218+304, none of the sources under study showed any significant  $\gamma$ -ray flare: they are thus not in conflict with a hadronic origin of the VHE emission. The flare of 1ES 1218+304 was characterized by

a time-scale of a day, which is still in agreement with the expected time-scales from hadronic models.

In general, in the proton-synchrotron scenario, we would expect a different temporal behaviour between the low-energy and high-energy components, with time lags due to the different acceleration and cooling time-scales of the leptonic and hadronic particle populations. The lepto-hadronic scenarios could exhibit different variability patterns even within the (very) high-energy range, due to the different contributions from the SSC and cascade components. The SSC component, more dominant in the *Fermi*-LAT energy range, would vary simultaneously with the electron-synchrotron emission.

A closer evaluation of variability would require detailed time-dependent modelling of the hadronic blazar emission, which is a complex problem, requiring a Monte-Carlo study of the  $p$ - $\gamma$  interactions and evolution of the associated cascades. Only recently Dimitrakoudis et al. (2012); Mastichiadis et al. (2013); Weidinger & Spanier (2013) presented the first results of time-dependent hadronic codes.

One of the open questions in blazar physics is the location of the  $\gamma$ -ray emitting region. For FSRQs and LBLs, in which the external photon field is important and the high-energy emission is dominated by EIC components, it is possible to constrain the location of the emitting region with respect to the SMBH environment, in particular the broad-line region and the accretion disk (see Cerruti et al. 2013b; Dermer et al. 2014). For HBLs it

**Table 4.** Parameters used for the hadronic modelling of our sources (lepto-hadronic scenario).

	1ES 0229+200	1ES 0347-121	RGB J0710+591	1ES 1101-232	1ES 1218+304
$z$	0.140	0.188	0.125	0.186	0.184
$\delta$	30	30	30	30	30
$R_{src}$ [ $10^{16}$ cm]	0.1 – 3.2	0.6 – 3.2	0.3 – 0.8	5.0 – 10	0.2 – 0.9
$B$ [G]	0.1 – 1.4	0.1 – 0.7	0.3 – 0.6	0.1 – 0.2	0.2 – 1.8
$*u_B$ [erg cm $^{-3}$ ]	$3.0 \times 10^{-4} - 0.08$	$6.2 \times 10^{-4} - 0.02$	$3.6 \times 10^{-3} - 0.01$	$(0.5 - 2.4) \times 10^{-3}$	$3.4 \times 10^{-3} - 0.1$
$\gamma_{e,min}$ [ $10^2$ ]	0.01	47 – 108	0.01	100 – 150	37 – 92
$\gamma_{e,break}$ [ $10^3$ ]	3.9 – 31	4.7 – 15	12 – 18	10 – 15	3.7 – 9.2
$\gamma_{e,max}$ [ $10^5$ ]	3.4 – 14	2.6 – 5.9	4.6 – 6.5	1.5 – 2.3	0.6 – 1.5
$\alpha_{e,1} = \alpha_{p,1}$	1.3	1.7	1.5	1.7	1.7
$\alpha_{e,2} = \alpha_{p,2}$	2.3	2.7	2.5	2.7	2.7
$K_e$ [cm $^{-3}$ ]	$5.6 \times 10^{-3} - 1.5$	2.9 – 135	2.7 – 29	0.5 – 3.5	26 – 2190
$*u_e$ [erg cm $^{-3}$ ]	$1.4 \times 10^{-5} - 2.2 \times 10^{-2}$	$4.2 \times 10^{-5} - 2.4 \times 10^{-3}$	$1.0 \times 10^{-3} - 9.2 \times 10^{-3}$	$7.3 \times 10^{-6} - 4.9 \times 10^{-5}$	$3.0 \times 10^{-4} - 0.03$
$\gamma_{p,min}$	1	1	1	1	1
$\gamma_{p,break}$ [ $10^9$ ]	$= \gamma_{p,max}$	$= \gamma_{p,max}$	$= \gamma_{p,max}$	$= \gamma_{p,max}$	$= \gamma_{p,max}$
$\gamma_{p,max}$ [ $10^9$ ]	0.06 – 0.3	0.15 – 0.45	0.1 – 0.15	0.6 – 1.0	0.1 – 0.4
$\eta = K_p/K_e$	0.1 – 0.8	0.1 – 0.3	0.04 – 0.1	0.05 – 0.1	0.1 – 0.4
$*u_p$ [erg cm $^{-3}$ ]	2.3 – 238	1.7 – 21	9.3 – 28	0.1 – 0.3	15 – 270
$*(u_p + u_e)/u_B$ [ $10^3$ ]	2.6 – 8.7	0.9 – 4.0	1.8 – 2.9	0.1 – 0.2	1.1 – 8.5
$*L$ [ $10^{45}$ erg s $^{-1}$ ]	4 – 57	15 – 44	3.9 – 12	17 – 27	12 – 42
$*min(\tau_{ad}; \tau_{syn}(\gamma_{p,max}))$ [hr]	19 – 590	120 – 590	56 – 150	$930 - 1.9 \times 10^3$	33 – 180

For a description, see Table 3.

is more difficult to estimate the location of the emitting region. One possibility is to assume a specific jet structure (conical) and that the emitting region fills the entire jet section. In this case  $R$  can be expressed as a function of the distance  $r$  from the central SMBH (see Ghisellini et al. 1985; Moderski et al. 2003; Potter & Cotter 2012). For the models presented here, assuming a conical jet with aperture angle  $\psi \simeq 10^\circ$  and  $r \simeq R/\tan\psi$ , we can estimate  $r \simeq 40 - 2000 R_G$  for the lepto-hadronic solutions, while for the proton-synchrotron models the location of the  $\gamma$ -ray emitting region is constrained to an even lesser degree, between 40 and  $2.5 \times 10^4 R_G$  (the lower values corresponding to lower power and closer to equipartition, with a limit at  $40 R_G$  due to our arbitrary choice of the minimum size of the emission region at  $10^{14-15}$  cm).

To reduce the number of free parameters of the models, we have related the maximum proton energy to the acceleration and cooling time-scales, and thus the magnetic field  $B$  and the size  $R$ . The maximum electron energy, on the other hand, is constrained by the X-ray observations, which sample the peak of the low-energy component of the SED. An important information on the acceleration mechanism can indeed be extracted from the ratio  $\gamma_{p,max}/\gamma_{e,max}$ : if the acceleration takes place in the Bohm diffusion regime at all energies, we expect  $\gamma_{p,max}/\gamma_{e,max} = m_p/m_e$  (or lower, if the maximum proton energy is determined by adiabatic losses instead of synchrotron losses). All our models are instead characterized by much higher ratios, which may indicate the presence of Kolmogorov or Kraichnan turbulence excited predominantly by the maximum energy protons. This is consistent with earlier studies, as discussed in Biermann

& Strittmatter (1987); Kolmogorov (1991); Kraichnan & Montgomery (1980); Mücke & Protheroe (2001, and references therein).

One of the main goals of AGN hadronic modeling is to study a potential link between photons and cosmic-rays or neutrinos detected at Earth. In particular, the detection in blazar spectra of emission associated with energetic protons would provide strong indication for AGN as the source of extra-galactic cosmic rays or high-energy neutrinos. In all our models, the maximum proton energy is around  $10^{18-19}$  eV (for the proton-synchrotron scenario, and one order of magnitude lower for the lepto-hadronic one). Under the simple hypothesis for the acceleration time-scale considered in this work,  $\gamma_{p,max}$  would thus not be sufficient to explain the most energetic cosmic rays (up to  $10^{20}$  eV) measured on Earth. On the other hand, these energies may still suffice for generating neutrinos in the PeV energy range that were recently discovered by the IceCube observatory. Further discussions of such implications are beyond the scope of this paper.

In recent years several authors (e.g. Essey & Kusenko 2010; Dermer et al. 2012; Murase et al. 2012; Tavecchio 2014) have studied the possibility that the blazar  $\gamma$ -ray emission is not produced at the source but rather along the path from the AGN to the observer. Observed  $\gamma$ -rays could be due to the interactions of cosmic-rays with the EBL and the CMB, and explain the detection of hard and distant blazars with IACTs as long as the intergalactic magnetic fields along the cosmic-ray propagation path are sufficiently weak. In our work, we did not consider this component, and implicitly made the assumption that the emission

at the source dominates over every other emission. Note that such contributions are expected to dominate for distant blazars, while all our sources are located at  $z < 0.2$ . Interestingly, there are no models in the literature studying both components (hadronic emission in the source and UHECR cascade in the path towards the observer); a self-consistent model linking the two contribution would be a natural evolution of the present code, and will be the object of further studies.

The observation of anomalous spectral components in the GeV-TeV energy band could represent a signature to distinguish hadronic models from (one-zone) SSC scenarios. As can be seen in Fig. 1, synchrotron emission by secondary cascades can produce a spectral hardening in the observed TeV spectrum, which would be hard to explain by standard SSC models. There is already some evidence for a hardening of the TeV emission seen in the VHE spectra of BL Lac objects (Horns & Meyer 2012; Inoue et al. 2013). Even though the current generation of Cherenkov telescopes probably would not be able to confirm this hard excess, such a feature could be clearly measurable with the future Cherenkov Telescope Array (CTA) (Actis et al. 2011; Sol et al. 2013), as shown by Zech & Cerruti (2013). A systematic study of the parameter space to estimate the strength of this "cascade-bump" as a function of the model parameters and the perspectives for CTA observations is currently in preparation and will be discussed in a separate publication.

Given the constraints described in Section 2.3, the (lepto-) hadronic modelling of UHBLs does not result in universal spectral features, but the coexistence of several spectral components at high energies in the lepto-hadronic scenario could lead to discernible shapes in certain cases. The emergence of additional components at intermediate energies — from cascade emission and proton-synchrotron photons (for low  $B$ -fields) — is another signature of these models, although difficult to detect due to a lack of instrumental coverage with sufficient sensitivity at energies below the *Fermi*-LAT band and above current X-ray telescopes. A combination of spectral and timing analysis with multi-wavelength data, including the large energy coverage at (very) high energies of CTA, will be the most promising approach to probe the different emission scenarios of these sources.

## 6 CONCLUSIONS

We propose an alternative interpretation of the SEDs of the currently known UHBLs, also known as EHBLs. Within a lepto-hadronic framework, their SEDs can be explained without the need for extreme Doppler factors (in all the models  $\delta$  was fixed equal to 30) or minimum Lorentz factors of the radiating particle distribution (which is around  $10^{2-3}$ , two order of magnitudes lower than that required by SSC models). A caveat of this interpretation is the very hard particle injection spectra required under the assumption of simple schemes for electron cooling and co-acceleration of leptons and protons, which may point to the operation of non-trivial physical mechanisms for such processes.

In a systematic approach, we have identified, for the first time, the complete parameter space in which hadronic interpretations of the high-energy bumps for the known UHBLs can be found. These solutions are grouped into two distinct regions in the B-R parameter space corresponding to the dominance of either

proton-synchrotron or p- $\gamma$ -induced cascade emission.

The hadronic solutions proposed here lead to values for the jet power that are generally sub-Eddington, in contrast to previous hadronic interpretations for the emission from other classes of blazars that often required highly super-Eddington values. On the other hand, they are several orders of magnitude away from equipartition between the proton energy density and magnetic field energy density. In our framework, acceleration to the highest observed energies of ultra-high energy cosmic rays is not expected for the sources under study, although they may possibly be of interest for the recently discovered high-energy neutrinos.

## ACKNOWLEDGMENTS

This work has made use of the computing capabilities of the Paris Observatory and the Harvard-Smithsonian Center for Astrophysics. The authors wish to thank Anita Reimer for providing the latest version of the *SOPHIA* code, as well as Hélène Sol for fruitful discussions, and the referee, Michael Zacharias, for the detailed report and the useful comments and remarks. The preliminary results of this project have been presented at several conferences and workshops: all the inputs from colleagues have significantly improved the present work, and are warmly acknowledged.

## References

- Abdo A. A., et al., 2010, *ApJ*, 716, 30
- Abdo A. A., et al., 2011, *ApJ*, 736, 131
- Acciari V. A., et al., 2009, *ApJ*, 703, 169
- Acciari V. A., et al., 2010a, *ApJL*, 709, L163
- Acciari V. A., et al., 2010b, *ApJL*, 715, L49
- Achterberg A., Gallant Y. A., Kirk J. G., Guthmann A. W., 2001, *MNRAS*, 328, 393
- Ackermann M., et al., 2013a, *ApJS*, 209, 34
- Ackermann M., et al., 2013b, *Science*, 339, 807
- Actis M., et al., 2011, *Experimental Astronomy*, 32, 193
- Aharonian F. A., Atoian A. M., Nagapetian A. M., 1983, *Astrofizika*, 19, 323
- Aharonian F., et al., 2002, *A&A*, 384, L23
- Aharonian F., et al., 2005, *A&A*, 437, 95
- Aharonian F., et al., 2006, *Nature*, 440, 1018
- Aharonian F., et al., 2007a, *A&A*, 470, 475
- Aharonian F., et al., 2007b, *A&A*, 473, L25
- Aharonian F., et al., 2007c, *ApJL*, 664, L71
- Aharonian F. A., Khargulyan D., Costamante L., 2008, *MNRAS*, 387, 1206
- Ahn C. P., et al., 2012, *ApJS*, 203, 21
- Albert J., et al., 2007, *ApJ*, 663, 125
- Aliu E., et al., 2014, *ApJ*, 782, 13
- Arlen T., et al., 2013, *ApJ*, 762, 92
- Asano K., Takahara F., Kusunose M., Toma K., Kakuwa J., 2014, *ApJ*, 780, 64
- Barkov M. V., Aharonian F. A., Bosch-Ramon V., 2010, *ApJ*, 724, 1517
- Barkov M. V., Aharonian F. A., Bogovalov S. V., Kelner S. R., Khargulyan D., 2012, *ApJ*, 749, 119
- Bednarz J., Ostrowski M., 1998, *Physical Review Letters*, 80, 3911

- Benbow W., 2011, Proc. of the 32nd ICRC, astro-ph/1110.0038,
- Biermann P. L., Strittmatter P. A., 1987, ApJ, 322, 643
- Blumenthal G. R., 1970, PhRD, 1, 1596
- Böttcher M., Reimer A., Sweeney K., Prakash A., 2013, ApJ, 768, 54
- Cao G., Wang J., 2014, ApJ, 783, 108
- Cavagnolo K. W., McNamara B. R., Nulsen P. E. J., Carilli C. L., Jones C., Bîrzan L., 2010, ApJ, 720, 1066
- Cerruti M., Boisson C., Zech A., 2013a, A&A, 558, A47
- Cerruti M., Dermer C. D., Lott B., Boisson C., Zech A., 2013b, ApJL, 771, L4
- Cerutti B., Uzdensky D. A., Begelman M. C., 2012, ApJ, 746, 148
- Chodorowski M. J., Zdziarski A. A., Sikora M., 1992, ApJ, 400, 181
- Costamante L., et al., 2001, A&A, 371, 512
- Dermer C. D., Atoyan A., 2001, Proc. of the 27th ICRC, astro-ph/0107200,
- Dermer C. D., Cavadini M., Razzaque S., Finke J. D., Chiang J., Lott B., 2011, ApJL, 733, L21
- Dermer C. D., Murase K., Takami H., 2012, ApJ, 755, 147
- Dermer C. D., Cerruti M., Lott B., Boisson C., Zech A., 2014, ApJ, 782, 82
- Dimitrakoudis S., Mastichiadis A., Protheroe R. J., Reimer A., 2012, A&A, 546, A120
- Djannati-Ataï A., et al., 2002, A&A, 391, L25
- Drury L. O., 1983, Reports on Progress in Physics, 46, 973
- Ellison D. C., Reynolds S. P., Jones F. C., 1990, ApJ, 360, 702
- Essey W., Kusenko A., 2010, Astroparticle Physics, 33, 81
- Falomo R., Carangelo N., Treves A., 2003, MNRAS, 343, 505
- Franceschini A., Rodighiero G., Vaccari M., 2008, A&A, 487, 837
- Ghisellini G., Maraschi L., Treves A., 1985, A&A, 146, 204
- H.E.S.S. Collaboration et al., 2012, A&A, 542, A94
- H.E.S.S. Collaboration et al., 2013, A&A, 550, A4
- Henri G., Saugé L., 2006, ApJ, 640, 185
- Horan D., et al., 2002, ApJ, 571, 753
- Horns D., Meyer M., 2012, JCAP, 2, 33
- IceCube Collaboration 2013, Science, 342, 1
- Inoue S., Takahara F., 1996, ApJ, 463, 555
- Inoue Y., Inoue S., Kobayashi M. A. R., Makiya R., Niino Y., Totani T., 2013, ApJ, 768, 197
- Jones F. C., 1968, Physical Review, 167, 1159
- Katarzyński K., Sol H., Kus A., 2001, A&A, 367, 809
- Katarzyński K., Ghisellini G., Tavecchio F., Gracia J., Maraschi L., 2006, MNRAS, 368, L52
- Kaufmann S., Wagner S. J., Tibolla O., Hauser M., 2011, A&A, 534, A130
- Kelner S. R., Aharonian F. A., 2008, PhRD, 78, 034013
- Kolmogorov A. N., 1991, Royal Society of London Proceedings Series A, 434, 9
- Konigl A., 1981, ApJ, 243, 700
- Kotera K., Olinto A. V., 2011, ARA&A, 49, 119
- Kraichnan R. H., Montgomery D., 1980, Reports on Progress in Physics, 43, 547
- Lefa E., Rieger F. M., Aharonian F., 2011, ApJ, 740, 64
- Leonardo E., et al., 2009, Proc. of the 31st ICRC, astro-ph/0907.0959,
- Lister M. L., et al., 2013, AJ, 146, 120
- Mannheim K., 1993, A&A, 269, 67
- Mastichiadis A., Petropoulou M., Dimitrakoudis S., 2013, MNRAS, 434, 2684
- Meyer M., Raue M., Mazin D., Horns D., 2012a, A&A, 542, A59
- Meyer E. T., Fossati G., Georganopoulos M., Lister M. L., 2012b, ApJL, 752, L4
- Moderski R., Sikora M., Błażejowski M., 2003, A&A, 406, 855
- Moore R. L., Stockman H. S., 1981, ApJ, 243, 60
- Mücke A., Protheroe R. J., 2001, Astroparticle Physics, 15, 121
- Mücke A., Engel R., Rachen J. P., Protheroe R. J., Stanev T., 2000, Computer Physics Communications, 124, 290
- Murase K., Dermer C. D., Takami H., Migliori G., 2012, ApJ, 749, 63
- Nolan P. L., et al., 2012, ApJS, 199, 31
- Padovani P., Giommi P., 1995, ApJ, 444, 567
- Petry D., et al., 2002, ApJ, 580, 104
- Potter W. J., Cotter G., 2012, MNRAS, 423, 756
- Protheroe R. J., Clay R. W., 2004, PASA, 21, 1
- Protheroe R. J., Johnson P. A., 1996, Astroparticle Physics, 4, 253
- Punch M., et al., 1992, Nature, 358, 477
- Rachen J. P., 2000, in Dingus B. L., Salamon M. H., Kieda D. B., eds, American Institute of Physics Conference Series Vol. 515, American Institute of Physics Conference Series. pp 41–52 (arXiv:astro-ph/0003282), doi:10.1063/1.1291342
- Remillard R. A., Tuohy I. R., Brissenden R. J. V., Buckley D. A. H., Schwartz D. A., Feigelson E. D., Tapia S., 1989, ApJ, 345, 140
- Reynoso M. M., Medina M. C., Romero G. E., 2011, A&A, 531, A30
- Rieger F. M., Bosch-Ramon V., Duffy P., 2007, ApSS, 309, 119
- Romero G. E., Torres D. F., Kaufman Bernadó M. M., Mirabel I. F., 2003, A&A, 410, L1
- Rüger M., Spanier F., Mannheim K., 2010, MNRAS, 401, 973
- Rybicki G. B., Lightman A. P., 1979, Radiative processes in astrophysics, Ed. Wiley-VCH
- Salamon M. H., Stecker F. W., 1998, ApJ, 493, 547
- Sikora M., Begelman M. C., Rees M. J., 1994, ApJ, 421, 153
- Sikora M., Stawarz Ł., Moderski R., Nalewajko K., Madejski G. M., 2009, ApJ, 704, 38
- Sironi L., Spitkovsky A., 2014, ApJL, 783, L21
- Sol H., et al., 2013, Astroparticle Physics, 43, 215
- Stein W. A., Odell S. L., Strittmatter P. A., 1976, ARA&A, 14, 173
- Tanaka Y. T., et al., 2014, astro-ph/1404.3727,
- Tavecchio F., 2014, MNRAS, 438, 3255
- Tavecchio F., Maraschi L., Ghisellini G., 1998, ApJ, 509, 608
- Tavecchio F., Ghisellini G., Ghirlanda G., Costamante L., Franceschini A., 2009, MNRAS, 399, L59
- Tavecchio F., Ghisellini G., Ghirlanda G., Foschini L., Maraschi L., 2010, MNRAS, 401, 1570
- Urry C. M., Padovani P., 1995, PASP, 107, 803
- Vainio R., Virtanen J. J. P., Schlickeiser R., 2003, A&A, 409, 821
- Virtanen J. J. P., Vainio R., 2005, ApJ, 621, 313
- Vovk I., Taylor A. M., Semikoz D., Neronov A., 2012, ApJL, 747, L14
- Weidinger M., Spanier F., 2010, A&A, 515, A18
- Weidinger M., Spanier F., 2013, in European Physical Journal Web of Conferences. p. 5009, doi:10.1051/epjconf/20136105009
- Woo J.-H., Urry C. M., van der Marel R. P., Lira P., Maza J., 2005, ApJ, 631, 762
- Zech A., Cerruti M., 2013, Proc. of the 33rd ICRC, astro-ph/1307.3038,
- Şentürk G. D., Errando M., Böttcher M., Mukherjee R., 2013, ApJ, 764, 119

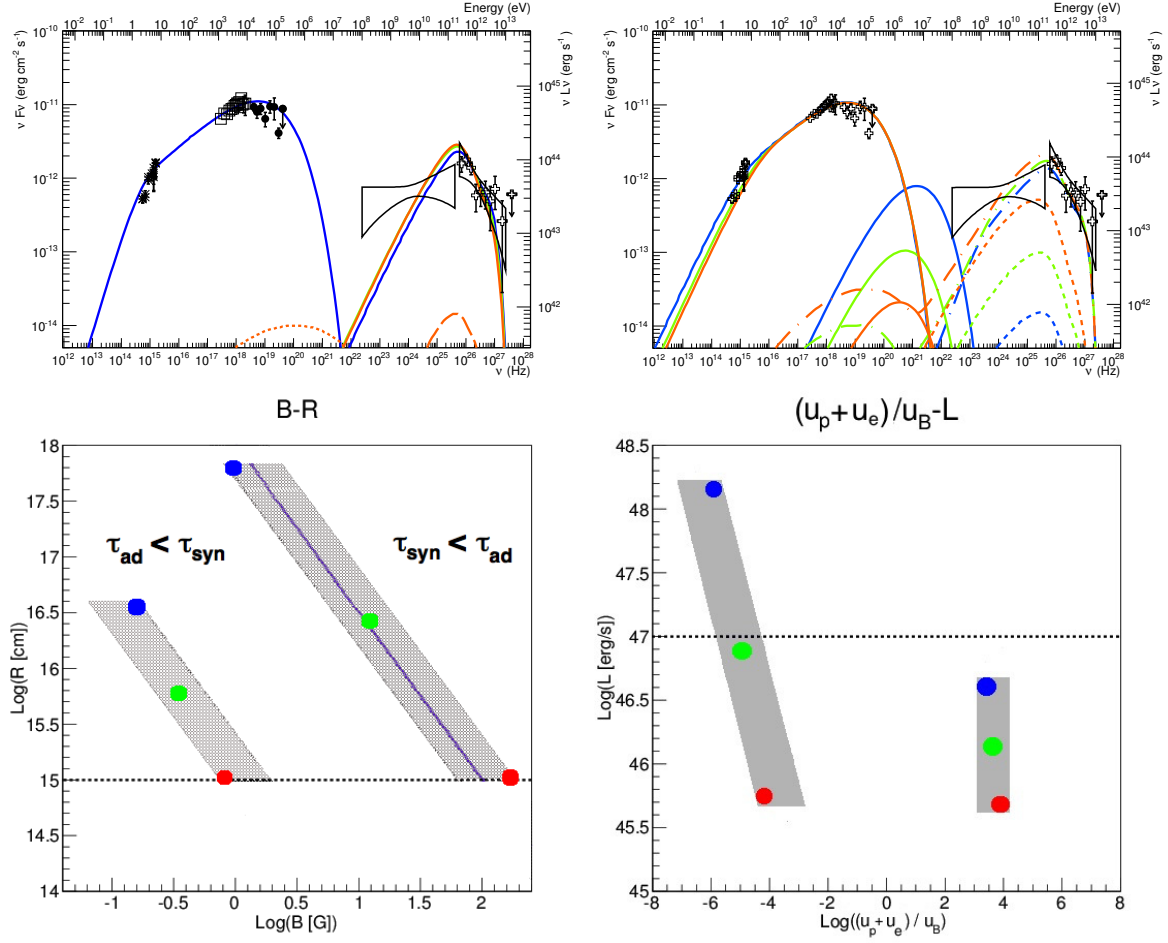


**Figure A1.** Same as Figure 2, for 1ES 0229+200, using data from Aliu et al. (2014). The values of the magnetic field and the emitting region size are  $(B[G], R[\text{cm}]) = (1, 6.8 \times 10^{17}), (13, 2.6 \times 10^{16}), (160, 1 \times 10^{15})$ , for the proton-synchrotron scenario, and  $(B[G], R[\text{cm}]) = (0.2, 3.2 \times 10^{16}), (0.3, 5.6 \times 10^{15}), (0.8, 1 \times 10^{15})$  for the lepto-hadronic scenario.

## APPENDIX A: FIGURES



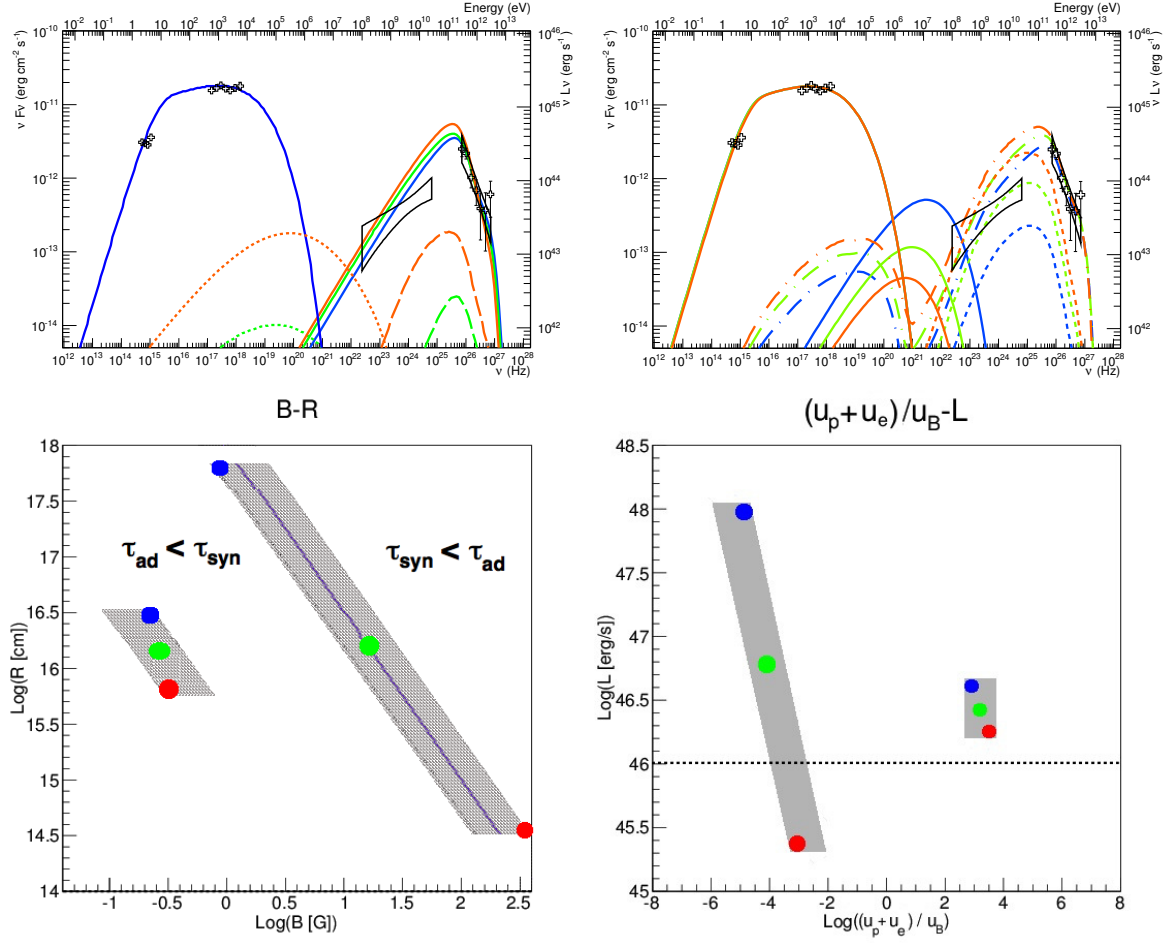


**Figure A2.** Same as Figure 2, for IES 0347-121, using data from Aharonian et al. (2007b). The values of the magnetic field and the emitting region size are  $(B[\text{G}], R[\text{cm}]) = (1, 6.5 \times 10^{17}), (17, 1.4 \times 10^{16}), (296, 3 \times 10^{14})$ , for the proton-synchrotron scenario, and  $(B[\text{G}], R[\text{cm}]) = (0.25, 3.2 \times 10^{16}), (0.3, 1.4 \times 10^{16}), (0.4, 6 \times 10^{15})$  for the lepto-hadronic scenario.

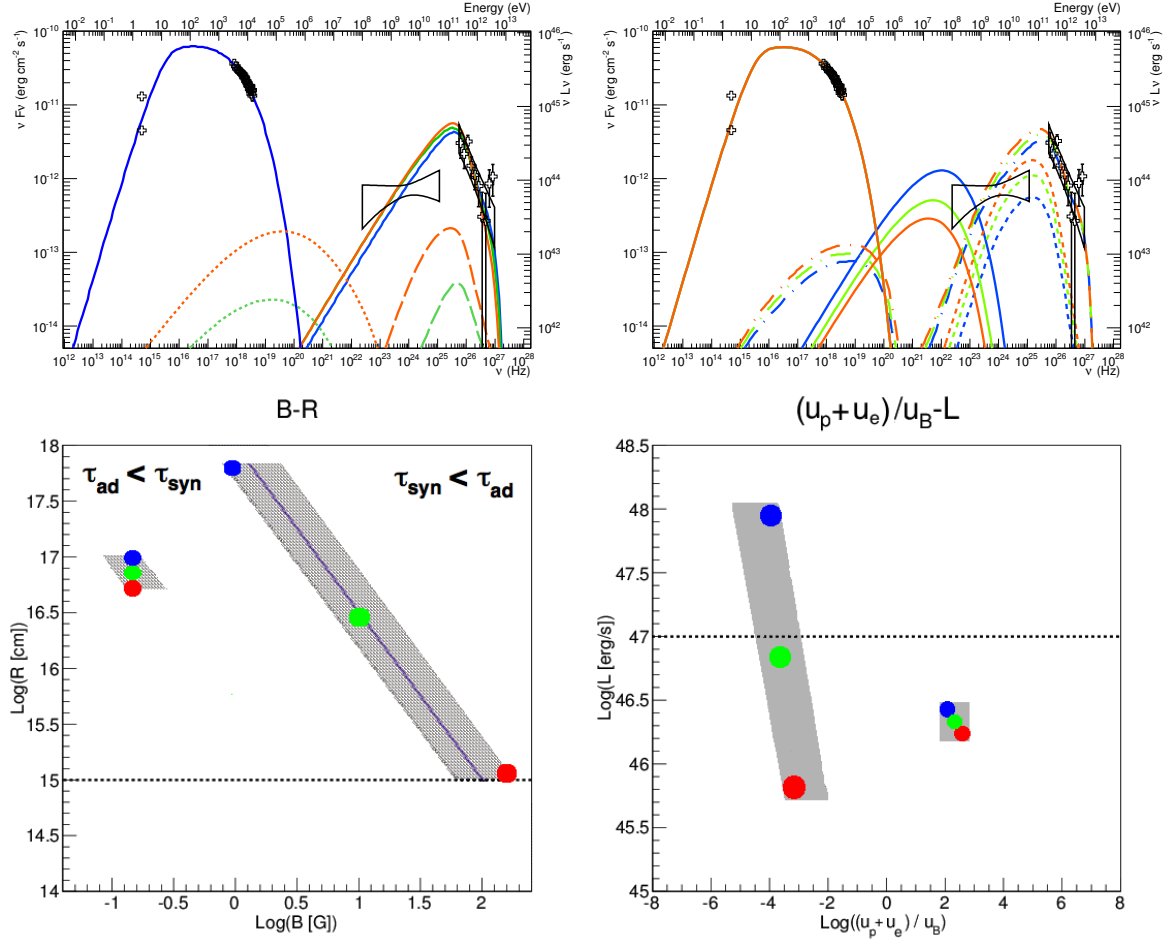


**Figure A3.** Same as Figure 2, for 1ES 1101-232, using data from Aharonian et al. (2007a). The two flux measurements in optical represent an estimation of the minimum and maximum flux from the AGN. The values of the magnetic field and the emitting region size are  $(B[\text{G}], R[\text{cm}]) = (1, 6.6 \times 10^{17}), (12, 2.6 \times 10^{16}), (133, 1 \times 10^{15})$ , for the proton-synchrotron scenario, and  $(B[\text{G}], R[\text{cm}]) = (0.15, 1 \times 10^{17}), (0.15, 7 \times 10^{16}), (0.15, 5 \times 10^{16})$  for the lepto-hadronic scenario.

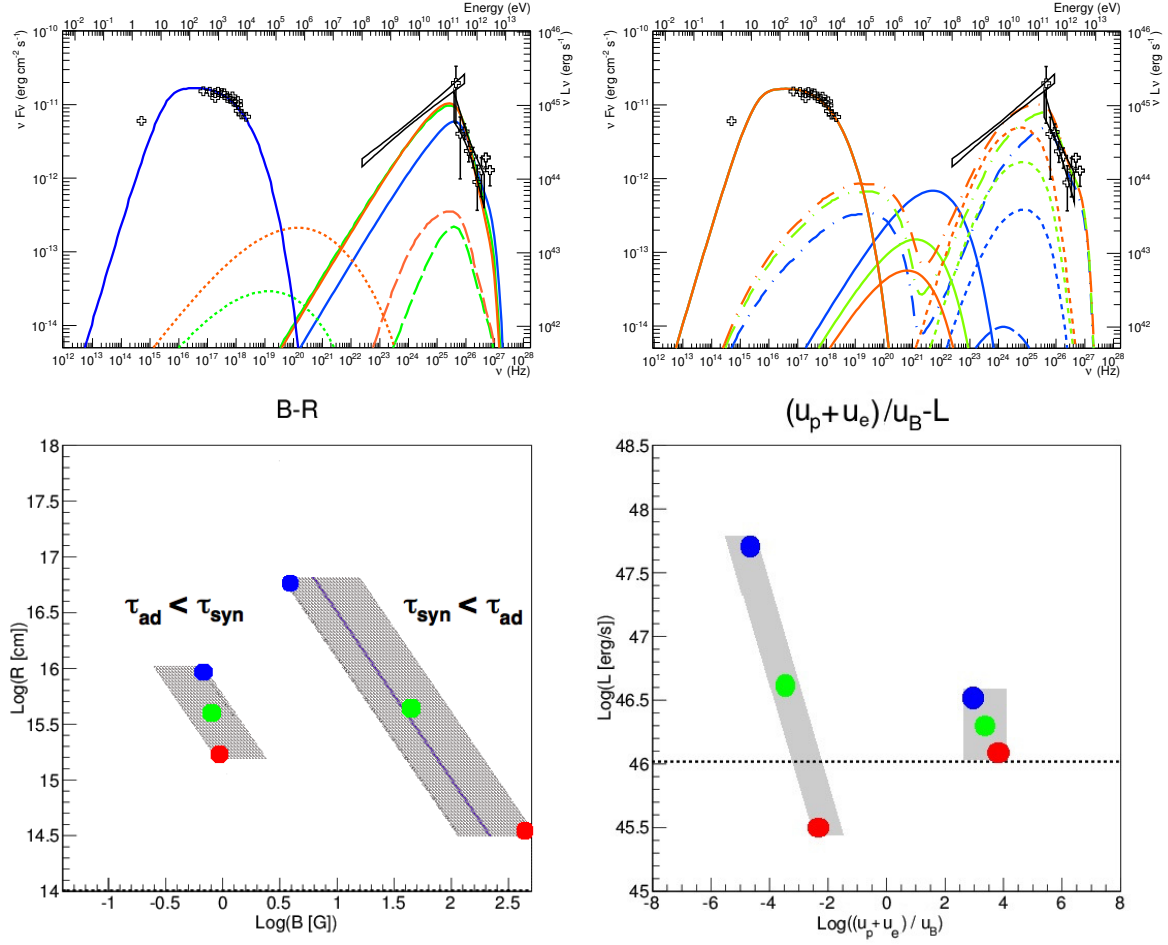


**Figure A4.** Same as Figure 2, for IES 1218+304, using data from R ger et al. (2010). The optical measurement includes the contamination from the host galaxy, and is considered as an upper limit of the AGN flux. The values of the magnetic field and the emitting region size are  $(B[G], R[cm]) = (3, 6.6 \times 10^{16}), (39, 4.5 \times 10^{15}), (454, 3 \times 10^{14})$ , for the proton-synchrotron scenario, and  $(B[G], R[cm]) = (0.5, 9 \times 10^{15}), (0.8, 4.2 \times 10^{15}), (1.2 \times 10^{15})$  for the lepto-hadronic scenario.